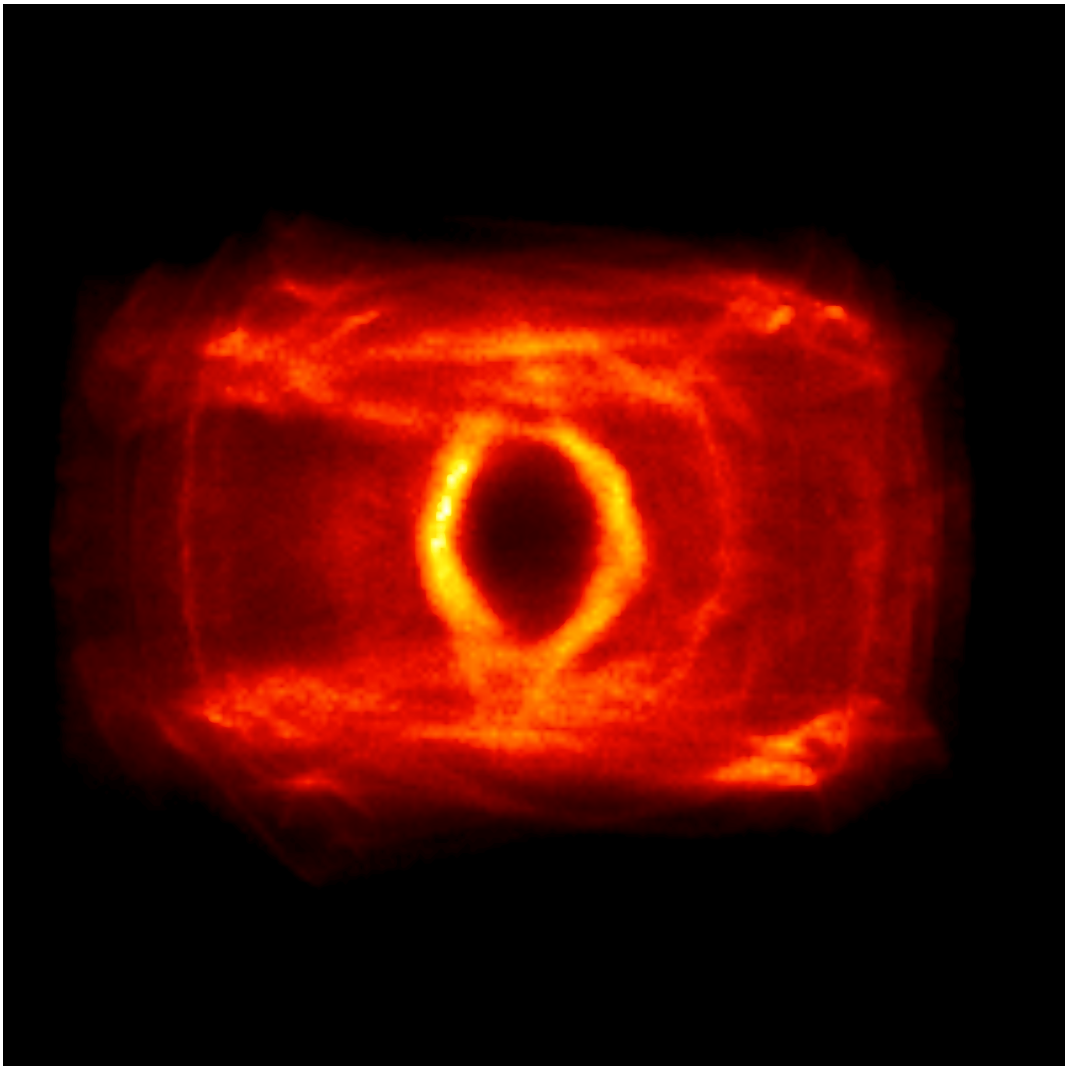

Plasma Instabilities in Ring and Bi-Maxwellian Electron Distributions

Thesis for the degree of Master of Science in Physics

ALBERT JOHANSSON

Department of Physics
CHALMERS UNIVERSITY OF TECHNOLOGY
Gothenburg, Sweden 2021

Plasma Instabilities in Ring and Bi-Maxwellian Electron Distributions

Author:
Albert Johansson

Supervisor:
Andréas Sundström
István Pusztai

2021
Gothenburg, Sweden

CHALMERS
UNIVERSITY OF TECHNOLOGY

Department of Physics
Division of Subatomic, High Energy and Plasma Physics
Plasma Theory

Plasma Instabilities in Ring and Bi-Maxwellian Electron Distributions

ALBERT JOHANSSON

Supervisor: Andréas Sundström, Department of Physics
István Pusztai, Department of Physics
Examiner: Tünde Fülöp, Department of Physics

Department of Physics
Division of Subatomic, High Energy and Plasma Physics, Plasma Theory
Chalmers University of Technology
SE-412 96 Gothenburg
Telephone: +46 (0)31 772 1000

Cover image: Electrostatically unstable 2D-momentum distribution of electrons as it collapses.

Typeset in LaTeX
Gothenburg, Sweden 2021

Plasma Instabilities in Ring and Bi-Maxwellian Electron Distributions

Albert Johansson

Department of Physics
Chalmers University of Technology

Abstract

Kinetic plasma instabilities affect a wide range of plasmas, from the small scales of laser-generated plasmas, up to the very largest scales of astrophysical plasmas. These instabilities depend on details of the velocity distribution of the particles. However, it is experimentally challenging to initialize the system with a sufficiently accurately known distribution function, that can be used for quantitative studies of kinetic instabilities. Recent results have shown the possibility of tailoring the velocity distribution through rapid ionization in laser-generated plasmas. Examples of such distribution functions are the bi-Maxwellian and the ring distributions. In this thesis, we have examined the electrostatic instability of a ring distribution function. It was found analytically that the ring distribution is electrostatically stable. Moreover, numerical simulations using the particle-in-cell approach show that certain incomplete (anisotropic) ring distributions can collapse to a complete (isotropic) ring distribution, through an electrostatic instability. In additional particle-in-cell simulations, we confirm the prediction of a previous analytical model of the effects of collisions on the Weibel instability of a bi-Maxwellian electron distribution. Using the previously known analytical model, it is found that collisions could play a major role in the Weibel instability in laboratory plasmas. We find that the evolution of the non-fluctuating part of the distribution is important during the time the instability grows to significant amplitudes. Thus, the strength of the seed fluctuations in the beginning of the simulation or experiment can impact the observed growth.

Keywords: plasma, 2D-isotropic electrostatic stability, two-stream instability, Weibel instability, collisions, particle-in-cell simulation

Acknowledgment

I would like to thank everybody at the Plasma Theory group at Chalmers for always being so friendly and helpful. Especially, I would like to thank Andréas and István for discussion sessions, always being available for questions and reading through the thesis. I can't express enough gratitude for the invaluable numerous times Andréas has read through the thesis. Special thanks to Tünde, who always wants the best of her students, and her relentless enthusiasm. I would also like to thank Julien for the nice coffee breaks, lunch sessions, and withstanding me and Andréas relentless talk about boats; Evangelos for the discussion about the two-stream instability; and Mathias for the ever so helpful tech support. It has always been a great pleasure working here! Moreover, this study would not have been possible without numerous previous work of others. The lecture notes by Alexander Schekochihin have been of great help for the physical understanding, and for the numerical simulations I owe both of the teams developing the Smilei code and Beskow cluster, respectively.

Albert Johansson, Gothenburg, 2020-05-27

Contents

Chapter 1

Introduction

The concept of an instability in physics is very broad. Generally, instabilities occur when a perturbation results in a positive feedback to itself. The perturbation will continue to grow, until some limiting process becomes active. A simple example is a ball on top of a hill. By perturbing the position from the top of the hill, gravitation accelerates the ball further downwards. It will move away from the top, with increasing velocity, until the hill ends. The position of the ball on the hilltop is unstable. In contrast, if the ball is at the bottom of a pit, a perturbation from that position yields a net acceleration towards the bottom of the pit. The displacement of the ball remains limited for finite input energy; the position of the ball is stable.

A plasma is simply put a gas of charged particles exhibiting collective behavior, which can host an amazingly large number of waves. Particularly, when particles are non-thermal, that is, are not in a local thermodynamic equilibrium, they can cause some of the waves supported by the system to be unstable. To describe such distributions, we use a kinetic formalism. This is a statistical description of the plasma which resolves both the momentum and position spaces of the particles.

A large class of instabilities is driven by an anisotropy of the velocity distribution of the plasma constituents, and appear in a wide range of environments, e.g. in solar corona (Marsch, 2006), intracluster medium (Roberg-Clark *et al.*, 2016), and Van Allen radiation belt (Horne *et al.*, 2007). Moreover, the Weibel instability (Weibel, 1959) can play a major role in the generation of the cosmological magnetic fields (Lazar *et al.*, 2009). These instabilities depend on details of the velocity distribution, and have been extensively studied theoretically.

Although many instabilities in a plasma have been studied theoretically, it is experimentally challenging to initialize the distribution function sufficiently accurately to study kinetic instabilities in the laboratory. Recently, Zhang *et al.* (2019) used intense ultra-short laser pulses to initialize the velocity distribution of electrons. The laser pulse can generate non-thermal velocity distributions

through rapid tunnel ionization. They focus on two such non-thermal distribution functions. A linearly polarized laser pulse can be used to obtain a so called bi-Maxwellian distribution; this is a Maxwellian distribution both parallel and orthogonal to the propagation direction, but with different thermal width. A circularly polarized laser pulse instead yields an electron velocity distribution resembling a ring in the plane of polarization.

Each diametrical cut of the ring distribution has two opposing flows. Thus one might naively expect it to be unstable to the so called two-stream electrostatic instability. In addition, the ring distribution has a temperature anisotropy that might be able to drive an electromagnetic instability. The stability properties of the ring distribution to electrostatic and electromagnetic modes is thus of interest for the interpretation of experiments.

In this thesis, we consider the electrostatic instability of a ring distribution, and show analytically that it is stable. This implies that any electrostatic instability signatures observed in experiments using a circularly polarized laser pulse must come from imperfections in the ring distribution. For example, these imperfections could be created at the boundary. We also studied a set of imperfections which break the isotropy of the distribution in the plane of the ring. We find by particle-in-cell simulations that distributions close to a ring, specifically "incomplete" ring distributions, collapse to one in an electrostatic instability (chapter 3).

The anisotropy of the ring or bi-Maxwellian distributions can destabilize the Weibel instability, which grows on a much longer time-scale than the electrostatic instabilities. On these time-scales, collisions may be non-negligible. Using particle-in-cell simulations, we confirm a previously known analytical model of the effects of collisions on the Weibel instability of a bi-Maxwellian electron distribution. This analytical model predicts that collisions can play a major role in laboratory plasmas. While the analytical model was known, our studies underline the importance of the (collisional) evolution of the non-fluctuating part of the distribution. This introduces a dependence of the growth dynamics on the strength of the seed fluctuations in the beginning of the simulation or experiment (chapter 4).

Chapter 2

Theory

In this chapter, we will first go through some basic theoretical concepts of plasma physics, which are required for later discussion. Then, we will dive into the electrostatic instabilities that can occur in the unmagnetized settings that we consider. We will continue on the path of instabilities and cover the basic theory behind the Weibel instability. Lastly, we will give a brief outlook on collisions, and finally end by introducing the particle-in-cell (PIC) approach to kinetic plasma modeling.

2.1 Basic Plasma Physics Concepts

Plasma physics is a rich field where systems consisting of charged particles exhibiting collective behavior are studied. Chen (1984) states the definition of a plasma as: "*a quasineutral gas of charged and neutral particles which exhibits collective behavior*". In a plasma, the physics is dominated by the electromagnetic interactions. These forces are long range: they affect many particles simultaneously. This leads to many particles moving coherently in a macroscopic fashion, hence the *collective behavior*. Plasmas are *quasineutral*, which means that the charge fluctuations in macroscopic volumes are much smaller than the total number of either charges, and the net charge is practically zero.

Since plasmas consist of free charged particles, these constituents will move and spatially distribute themselves to counteract external electric fields. This shielding is not perfect, since the particles have some random thermal movement. The phenomenon is called *Debye shielding*, and the characteristic length scale of the shielding is called the *Debye length*, λ_{D}. The electromagnetic field from a charged particle located at the center of a sphere of radius λ_{D}, the *Debye sphere*, will inside this sphere resemble its unshielded form. By its nature, Debye shielding is a statistical phenomenon caused by many particles. Therefore, there must be many particles inside the Debye sphere, and for many plasmas of interest, this is

indeed the case. Debye shielding is also the main reason the gas is quasineutral. When the length scale of the system is much larger than the Debye length, low-frequency electric fields are shielded from the plasma, and charge fluctuations are confined to smaller volumes; and the overall plasma is quasineutral.

For the plasma to be dominated by electromagnetic interactions, it is not sufficient that there are many particles in the Debye sphere. It is also necessary that the interactions, *collisions*, between individual particles that contribute to the plasma dynamics are of electromagnetic nature. Scattering events due to the Coulomb force are called *Coulomb collisions*. There can also be collisions with neutral particles. For the dynamics to be driven by electromagnetic forces, the dynamics should mostly be affected by the Coulomb collisions.

To summarize, a plasma is a quasineutral gas exhibiting collective behavior. This is fulfilled when three criteria are satisfied. Firstly, there must be many particles within the Debye sphere. Secondly, the length scale of the system must be much larger than the Debye length. Finally, the collisions should mostly be of electromagnetic nature.

2.1.1 Distribution Function

As many particles are inside the Debye sphere, thus in any finite volume of interest, it is particularly useful to employ a statistical description of the different plasma particle species, and describe them by their respective *distribution function*, denoted f. The distribution function is a measure of the phase-space density of particles with a specific velocity $\boldsymbol{v}$ at position $\boldsymbol{x}$ and time t. Phase space is the six-dimensional space spanned by the position and momentum of the particles. If we are specific about a species, denoted by α, we use a subscript. That is, f_α is the distribution function of species α. In this thesis we will normalize the distribution function such that its velocity integral yields the number density of the species in space $n_\alpha(\boldsymbol{x})$,

$$n_\alpha(\boldsymbol{x}) = \int f_\alpha \mathrm{d}^3 v. \tag{2.1}$$

Then $f_\alpha(\boldsymbol{x}, \boldsymbol{v}, t)\mathrm{d}^3 v \mathrm{d}^3 x$ is the number of particles in the infinitesmal phase-space volume $\mathrm{d}^3 v \mathrm{d}^3 x$, centered around the position $\boldsymbol{x}$ and velocity $\boldsymbol{v}$ at time t.

2.1.2 Vlasov Equation

The path that a single particle, of charge q, would take in phase space is governed by Newton's equations of motion. We will denote this path by $\boldsymbol{x}(t)$, $\boldsymbol{v}(t)$. Along this path, the distribution function must be constant, as no particles can be created or destroyed. Thus the total time (convective) derivative of the distribution

function along this path must be 0,

$$0 = \frac{\mathrm{d}f(\boldsymbol{x}(t), \boldsymbol{v}(t), t)}{\mathrm{d}t} = \frac{\partial f}{\partial t} + \frac{\mathrm{d}\boldsymbol{x}(t)}{\mathrm{d}t} \cdot \frac{\partial f}{\partial \boldsymbol{x}} + \frac{\mathrm{d}\boldsymbol{v}(t)}{\mathrm{d}t} \cdot \frac{\partial f}{\partial \boldsymbol{v}}. \tag{2.2}$$

We know that the derivative of position with respect to (w.r.t.) time is the velocity, $\mathrm{d}\boldsymbol{x}/\mathrm{d}t = \boldsymbol{v}$. The derivative of the velocity w.r.t. time is the acceleration. Using Newton's second law of motion and replacing the force with the Lorentz force, the acceleration can be expressed as $\mathrm{d}\boldsymbol{v}/\mathrm{d}t = (q/m)(\boldsymbol{E} + \boldsymbol{v} \times \boldsymbol{B})$, where q is the charge of the particles, m is their mass, $\boldsymbol{E}$ is the electric field, and $\boldsymbol{B}$ is the magnetic field. Combining these two observations, the equation above can be rewritten as

$$\frac{\partial f}{\partial t} + \boldsymbol{v} \cdot \frac{\partial f}{\partial \boldsymbol{x}} + \frac{q}{m}(\boldsymbol{E} + \boldsymbol{v} \times \boldsymbol{B}) \cdot \frac{\partial f}{\partial \boldsymbol{v}} = 0. \tag{2.3}$$

The distribution function could, in principle, be expressed by the exact position and momentum of each particle. This is equivalent to treating the particles individually, which is, due to the shear amount of particles, impractical. Instead, we will use coarse-graining to average the fields over some length scale much smaller than the Debye length, but large enough to include enough particles to be statistically meaningful. Then the macroscopic physics is captured in an averaged distribution function.[1] This coarse-graining is possible due to the condition that many particles must be within the Debye sphere.

However, just replacing fields and the distribution with their averages fails to describe some of the granular effects from individual particles, in other words, the microscopic fluctuations. These microscopic effects are summarized in a collision operator, $C\{\cdot\}$, which describes the effect of collisions on the distribution function. The form of this operator depends on the physical properties of the system, and has been derived in several different limits. With all this in mind, the statistically averaged kinetic equation, so called Vlasov equation, reads

$$\frac{\partial \langle f_\alpha \rangle}{\partial t} + \boldsymbol{v} \cdot \frac{\partial \langle f_\alpha \rangle}{\partial \boldsymbol{x}} + \frac{q_\alpha}{m_\alpha}(\langle \boldsymbol{E} \rangle + \boldsymbol{v} \times \langle \boldsymbol{B} \rangle) \cdot \frac{\partial \langle f_\alpha \rangle}{\partial \boldsymbol{v}} = C\{\langle f_\alpha \rangle\}, \tag{2.4}$$

where the collision operator should preserve total energy and momentum as well as the number of particles of the colliding particle pairs. The average brackets refer to the coarse-graining, or ensemble averages. We will henceforth drop these brackets, that is, $\langle A \rangle = A$ for quantity A. These equations are then coupled with

[1] Formally a generalization of the BBGKY procedure is employed, and will not be discussed here. Intuitively, we can view it as an ensemble average over many systems with different initial values.

Maxwell's equations,

$$\begin{aligned} \boldsymbol{\nabla} \cdot \boldsymbol{E} &= \frac{\rho}{\epsilon_0}, & \boldsymbol{\nabla} \times \boldsymbol{E} &= -\frac{\partial \boldsymbol{B}}{\partial t}, \\ \boldsymbol{\nabla} \cdot \boldsymbol{B} &= 0, & \boldsymbol{\nabla} \times \boldsymbol{B} &= \mu_0 \boldsymbol{J} + \mu_0 \epsilon_0 \frac{\partial \boldsymbol{E}}{\partial t}, \end{aligned} \tag{2.5}$$

through

$$\rho = \sum_\alpha \int q_\alpha f_\alpha \, \mathrm{d}^3 v \quad \text{and} \quad \boldsymbol{J} = \sum_\alpha \int q_\alpha \boldsymbol{v} f_\alpha \, \mathrm{d}^3 v \,, \tag{2.6}$$

and form a closed set of equations. Note that Maxwell's equations are the same for the coarse-grained fields as for the microscopic fields.

2.1.3 Averages

In this thesis, we will use several types of averages. These include a spatial average, a fluid average, and an average over all particles. The spatial average of some quantity A, denoted by brackets and a subscript x, is defined as

$$\langle A \rangle_x \equiv \frac{\int A \mathrm{d}^3 x}{\int \mathrm{d}^3 x}, \tag{2.7}$$

where the spatial volume being integrated over is the whole plasma volume. We can also talk about the fluid average of the physical quantity A for species α, denoted by brackets, superscript "fluid" and subscript α. This is defined as

$$\langle A \rangle_\alpha^{\text{fluid}} (\boldsymbol{x}) \equiv \frac{1}{\int f_\alpha \mathrm{d}^3 v} \int A f_\alpha \mathrm{d}^3 v. \tag{2.8}$$

This average corresponds to the average value of A over each particle located at $\boldsymbol{x}$.

The average of quantity A over all particles of species α is denoted with brackets, superscript "part", and a subscript α. This average is defined by

$$\langle A \rangle_\alpha^{\text{part}} \equiv \frac{\int A(t, \boldsymbol{x}, \boldsymbol{v}) f_\alpha \mathrm{d}^3 v \mathrm{d}^3 x}{\int f_\alpha \mathrm{d}^3 v \mathrm{d}^3 x} \approx \frac{1}{N} \sum_{i=1}^{N} A_{i\alpha} \tag{2.9}$$

where $A_{i\alpha}$ is the microscopic quantity A for particle i out of N, of species α, at time t, and $A(t, \boldsymbol{x}, \boldsymbol{v})$ is the coarse-graining of quantity A. Note that in the case of small density fluctuations, and when A depends only on velocity, $\langle A \rangle_\alpha^{\text{part}}$ coincides with the fluid average. This particle average is useful in, for example, the particle-based numerical modeling approach that we will later use.

2.2 Electrostatic Instabilities

In this section, we will derive the linear properties of electrostatic instabilities in a collisionless, unmagnetized plasma. This will be done by perturbing some equilibrium distribution. We will mainly follow the derivation by Landau (1946), with some additional explanatory steps, along the lines of the lecture notes by Schekochihin (2021).

To better understand what an equilibrium distribution is, consider a 1D equilibrium distribution f_0 that satisfies $\partial f_0/\partial t = 0$, and consider the case when it is separable, that is, $f_0(x, v) = X(x)V(v_x)$. Using the electrostatic potential $E = -\,\mathrm{d}\phi_x(x)/\mathrm{d}x$, the Vlasov equation reads (unless $\mathrm{d}\phi_x/\mathrm{d}x \equiv 0$)

$$\frac{1}{q\frac{\mathrm{d}\phi_x}{\mathrm{d}x}}\frac{\frac{\partial X}{\partial x}}{X} = \frac{1}{mv}\frac{\frac{\partial V}{\partial v_x}}{V}. \tag{2.10}$$

The l.h.s. depends only on x and the r.h.s. depends only on v_x. As these are phase-space coordinates, they are independent variables. Therefore, each side must be constant. It will soon be apparent that the distribution is in thermal equilibrium and the constant is $-\beta = -1/(k_B T)$ where k_B is Boltzmann's constant and T the temperature. Equating the l.h.s. and r.h.s. independently to the constant $-\beta$ and solving the differential equation yields our distribution function as

$$f_{0x} = N \exp\left(-\frac{q\phi_x}{k_B T}\right) \exp\left(-\frac{m v_x^2}{2k_B T}\right), \tag{2.11}$$

where N is some normalization constant. In fact, if $\boldsymbol{E} = -\,\mathrm{d}\phi/\mathrm{d}\boldsymbol{x} \neq 0$ almost everywhere, then the general solution to an electrostatic equilibrium distribution is given by any function of the energy,

$$f(\boldsymbol{x}, \boldsymbol{v}) = f\left(\frac{1}{2}m\boldsymbol{v}^2 + q\phi\right), \tag{2.12}$$

regardless of the number of dimensions. This can be checked by substituting it into the Vlasov equation. If, on the other hand, $\mathrm{d}\phi/\mathrm{d}\boldsymbol{x} \equiv 0$, then $\boldsymbol{E} = 0$, and from the Vlasov equation we obtain $\partial f_0/\partial \boldsymbol{x} = 0$. In other words, the distribution is homogeneous in space, and there is no criteria on the velocity distribution.

Consider the unmagnetized, collisionless, electrostatic Vlasov equation given by

$$\frac{\partial f_\alpha}{\partial t} + \boldsymbol{v} \cdot \frac{\partial f_\alpha}{\partial \boldsymbol{x}} + \frac{q_\alpha}{m_\alpha}\boldsymbol{E} \cdot \frac{\partial f_\alpha}{\partial \boldsymbol{v}} = 0. \tag{2.13}$$

We introduce a inhomogeneous part to the distribution function as a small perturbation. It is convenient to work with a plane-wave decomposition of the distribution function,

$$f_\alpha(\boldsymbol{x}, \boldsymbol{v}, t) = f_{0\alpha}(\boldsymbol{v}, t) + \sum_{\boldsymbol{k}\neq 0} f_{\boldsymbol{k}\alpha}(\boldsymbol{v}, t) \exp(i\boldsymbol{k}\cdot\boldsymbol{x}), \tag{2.14}$$

where $f_{\boldsymbol{k}\alpha}(\boldsymbol{v}, t)$ is given by

$$f_{\boldsymbol{k}\alpha}(\boldsymbol{v}, t) = \langle f_\alpha(\boldsymbol{x}, \boldsymbol{v}, t) \exp(-i\boldsymbol{k}\cdot\boldsymbol{x})\rangle_x , \tag{2.15}$$

and together yield the introduced perturbation. Note that as $f_{0\alpha}$ is homogeneous in space, it is an electrostatic equilibrium distribution.

We will work with the electrostatic potential ϕ, for which $\boldsymbol{E} = -\boldsymbol{\nabla}\phi$. The integration constant for ϕ is chosen such that the average of ϕ is 0. This choice is quite convenient, as in Fourier space ϕ has only components with nonzero $\boldsymbol{k}$. We will work with the plane wave representation of the electrostatic potential,

$$\phi(\boldsymbol{x}, t) = \sum_{\boldsymbol{k}\neq 0} \phi_{\boldsymbol{k}}(t) \exp(i\boldsymbol{k}\cdot\boldsymbol{x}), \tag{2.16}$$

where $\phi_{\boldsymbol{k}}(t)$ is given by

$$\phi_{\boldsymbol{k}}(t) = \langle \phi(\boldsymbol{x}, t) \exp(-i\boldsymbol{k}\cdot\boldsymbol{x})\rangle_x . \tag{2.17}$$

When working with plane waves, we introduce a rectangular box of finite length, hidden in which values of $\boldsymbol{k}$ are allowed in the sum. If the box is taken be of infinite length, then the sum is replaced with an integral instead. However, we will later look at the projection onto a single basis vector $\exp(i\boldsymbol{k}\cdot\boldsymbol{x})$, and then this difference is irrelevant. Also note that when perturbations are small, we may consider each of them independently in the linear limit.

Substituting eqs. (2.14) and (2.16) into eq. (2.13), we obtain

$$\begin{aligned} 0 = {} & \frac{\partial f_{0\alpha}}{\partial t} + \sum_{\boldsymbol{k}\neq 0} \exp(i\boldsymbol{k}\cdot\boldsymbol{x}) \frac{\partial f_{\boldsymbol{k}\alpha}}{\partial t} \\ & + \sum_{\boldsymbol{k}} \boldsymbol{v}\cdot(i\boldsymbol{k}\exp(\boldsymbol{k}\cdot\boldsymbol{x}) f_{\boldsymbol{k}\alpha}) \\ & + \frac{q}{m_\alpha}\left(\sum_{\boldsymbol{k}} -i\boldsymbol{k}\phi_{\boldsymbol{k}} \exp(i\boldsymbol{k}\cdot\boldsymbol{x})\right)\cdot\left(\frac{\partial f_0}{\partial \boldsymbol{v}} + \sum_{\boldsymbol{k}\neq 0} \exp(i\boldsymbol{k}\cdot\boldsymbol{x}) \frac{\partial f_{\boldsymbol{k}\alpha}}{\partial \boldsymbol{v}}\right). \end{aligned} \tag{2.18}$$

When considering linear theory, the perturbations are small compared to the mean,

$f_{\boldsymbol{k},\alpha} \ll f_{0\alpha}$, so we may neglect second order terms, yielding

$$\begin{aligned} 0 = &\frac{\partial f_{0\alpha}}{\partial t} + \sum_{\boldsymbol{k}\neq 0} \frac{\partial f_{\boldsymbol{k}\alpha}}{\partial t} \exp(i\boldsymbol{k}\cdot\boldsymbol{x}) \\ &+ \sum_{\boldsymbol{k}} \boldsymbol{v}\cdot i\boldsymbol{k} f_{\boldsymbol{k}\alpha} \exp(i\boldsymbol{k}\cdot\boldsymbol{x}) \\ &- \frac{q}{m_\alpha} \sum_{\boldsymbol{k}} i\phi_{\boldsymbol{k}} \exp(i\boldsymbol{k}\cdot\boldsymbol{x}) \boldsymbol{k}\cdot\frac{\partial f_{0\alpha}}{\partial \boldsymbol{v}}. \end{aligned} \tag{2.19}$$

This equation is also satisfied for each basis vector individually, as the set of $\exp(i\boldsymbol{k}\cdot\boldsymbol{x})$ is orthogonal in the L^2-function space. The equation projected onto a single $\exp(i\boldsymbol{k}\cdot\boldsymbol{x})$ for non-zero $\boldsymbol{k}$ gives

$$0 = \frac{\partial f_{\boldsymbol{k}\alpha}}{\partial t} + \boldsymbol{v}\cdot(i\boldsymbol{k} f_{\boldsymbol{k}\alpha}) - \frac{q}{m_\alpha} i\phi_{\boldsymbol{k}} \boldsymbol{k}\cdot\frac{\partial f_{0\alpha}}{\partial \boldsymbol{v}}. \tag{2.20}$$

Projection onto the basis vector given by $\boldsymbol{k} = \boldsymbol{0}$ instead yields $\partial f_{0\alpha}/\partial t = 0$. Retaining second-order terms would yield a non-zero time derivative of $f_{0\alpha}$.

As we are interested in the evolution of perturbations, we will solve eq. (2.20) as an initial value problem. It is therefore convenient to Laplace transform our equation to the dual time variable p. This is guaranteed to converge when the function in question grows slower than $\exp(\sigma t)$, for some real σ. The real part of p must be sufficiently large, in the sense that $\mathrm{Re}(p) \geq \sigma$. The Laplace transform is given by

$$\mathcal{L}\{h\} = \int_0^\infty h \exp(-pt)\mathrm{d}t, \tag{2.21}$$

and its inverse by

$$\mathcal{L}^{-1}\{\hat{h}\} = \frac{1}{2\pi i} \int_{-i\infty+\sigma}^{i\infty+\sigma} \hat{h} \exp(pt)\mathrm{d}p. \tag{2.22}$$

We denote the Laplace-transformed variables with a hat, $\mathcal{L}\{f_{\boldsymbol{k}\alpha}\} = \hat{f}_{\boldsymbol{k}\alpha}$.

Let the initial perturbation for some species α be $f_{\boldsymbol{k}\alpha}(\boldsymbol{v}, 0) = g_{\boldsymbol{k}\alpha}(\boldsymbol{v})$. Laplace transforming eq. (2.20), we obtain

$$0 = g_{\boldsymbol{k}\alpha} + p\hat{f}_{\boldsymbol{k}\alpha} + \boldsymbol{v}\cdot(i\boldsymbol{k}\hat{f}_{\boldsymbol{k}\alpha}) - \frac{q_\alpha}{m_\alpha} i\hat{\phi}_{\boldsymbol{k}} \boldsymbol{k}\cdot\frac{\partial f_{0\alpha}}{\partial \boldsymbol{v}}. \tag{2.23}$$

This is a linear equation in $\hat{f}_{\boldsymbol{k}\alpha}$. Solving for $\hat{f}_{\boldsymbol{k}\alpha}$, we obtain

$$\hat{f}_{\boldsymbol{k}\alpha} = \frac{1}{p + i\boldsymbol{v}\cdot\boldsymbol{k}} \left(\frac{q_\alpha}{m_\alpha} \hat{\phi}_{\boldsymbol{k}} i\boldsymbol{k}\cdot\frac{\partial f_{0\alpha}}{\partial \boldsymbol{v}} + g_{\boldsymbol{k}\alpha} \right). \tag{2.24}$$

Now, we need to couple this with Maxwell's equations to form a closed set of equations. As we are treating the problem electrostatically, we have Poisson's equation,

$$\nabla^2\phi(\boldsymbol{x},t) = -\frac{\rho(\boldsymbol{x},t)}{\epsilon_0} = -\sum_\alpha \frac{q_\alpha}{\epsilon_0}\int f_\alpha(\boldsymbol{x},\boldsymbol{v},t)\mathrm{d}^3\boldsymbol{v}, \tag{2.25}$$

where we expressed the charge density as a sum of the charge moments over all species in the plasma. With eqs. (2.14) and (2.16), we can now express eq. (2.25) as

$$-\sum_{\boldsymbol{k}} k^2\phi_{\boldsymbol{k}}\exp(i\boldsymbol{k}\cdot\boldsymbol{x}) = -\sum_\alpha \frac{q_\alpha}{\epsilon_0}\int\left(f_{0\alpha}+\sum_{\boldsymbol{k}} f_{\boldsymbol{k}\alpha}\exp(i\boldsymbol{k}\cdot\boldsymbol{x})\right)\mathrm{d}^3\boldsymbol{v}, \tag{2.26}$$

where we have introduced $k = |\boldsymbol{k}|$. By projecting on a single plane wave, we obtain that it holds for each $\boldsymbol{k}$ individually. Laplace transforming Poisson's equation, and noting that the only time dependence is in $\phi_{\boldsymbol{k}\alpha}$ and $f_{\boldsymbol{k}\alpha}$, yields

$$k^2\hat{\phi}_{\boldsymbol{k}} = \sum_\alpha \frac{q_\alpha}{\epsilon_0}\int \hat{f}_{\boldsymbol{k}\alpha}\mathrm{d}^3\boldsymbol{v}, \tag{2.27}$$

for nonzero $\boldsymbol{k}$. Substituting the expression for $\hat{f}_{\boldsymbol{k}}$ in eq. (2.24) results in

$$\epsilon_0 k^2\hat{\phi}_{\boldsymbol{k}} = \sum_\alpha q_\alpha\int\frac{1}{p+i\boldsymbol{v}\cdot\boldsymbol{k}}\left(\frac{q_\alpha}{m_\alpha}\hat{\phi}_{\boldsymbol{k}}i\boldsymbol{k}\cdot\frac{\partial f_{0\alpha}}{\partial\boldsymbol{v}}+g_{\boldsymbol{k}\alpha}\right)\mathrm{d}^3\boldsymbol{v}, \tag{2.28}$$

and solving for $\hat{\phi}_{\boldsymbol{k}}$ yields

$$\left(1-\sum_\alpha\frac{q_\alpha^2}{m_\alpha\epsilon_0 k^2}\int\frac{\boldsymbol{k}\cdot\frac{\partial f_{0\alpha}}{\partial\boldsymbol{v}}}{\boldsymbol{v}\cdot\boldsymbol{k}-ip}\mathrm{d}^3\boldsymbol{v}\right)\hat{\phi}_{\boldsymbol{k}} = \frac{1}{k^2}\sum_\alpha\frac{q_\alpha}{\epsilon_0}\int\frac{g_{\boldsymbol{k}\alpha}}{p+i\boldsymbol{v}\cdot\boldsymbol{k}}\mathrm{d}^3\boldsymbol{v}. \tag{2.29}$$

We are now free to choose our coordinate system and can thus align the x axis with the $\boldsymbol{k}$ vector. This means that $\boldsymbol{k}\cdot\partial f_{0\alpha}/\partial\boldsymbol{v} = k\,\partial f_{0\alpha}/\partial v_x$, and $\boldsymbol{v}\cdot\boldsymbol{k} = v_x k$. Thus the integral can be expressed as

$$\begin{aligned}\int\frac{\boldsymbol{k}\cdot\frac{\partial f_{0\alpha}}{\partial\boldsymbol{v}}}{\boldsymbol{v}\cdot\boldsymbol{k}-ip}\mathrm{d}^3\boldsymbol{v} &= \iiint\frac{k\frac{\partial f_{0\alpha}}{\partial v_x}}{v_x k-ip}\mathrm{d}v_x\mathrm{d}v_y\mathrm{d}v_z\\ &= \int\frac{k}{v_x k-ip}\frac{\mathrm{d}}{\mathrm{d}v_x}\iint f_{0\alpha}\mathrm{d}v_y\mathrm{d}v_z\mathrm{d}v_x\\ &= \int\frac{k f'_{0\alpha}(v_x)}{v_x k-ip}\mathrm{d}v_x.\end{aligned} \tag{2.30}$$

Here $f_{0\alpha}(v_x)$ is the marginal distribution in v_x to the joint distribution $f_{0\alpha} = f_{0\alpha}(v_x,v_y,v_z)$, and $f'_{0\alpha}(v_x)$ its derivative w.r.t. v_x.

By examining eq. (2.29), we see that the potential times some function dependent on p and k equals the time evolution of the initial charge distribution. If $f_{0\alpha}$ is analytical, and the same is true for $g_{\boldsymbol{k}\alpha}$, then both integrals must also be analytical. Then $\phi_{\boldsymbol{k}}$ is analytical everywhere except where the prefactor of $\hat{\phi}_{\boldsymbol{k}}$ is 0. The prefactor of $\hat{\phi}_{\boldsymbol{k}}$ is called the *dielectric function* $\epsilon(p,k)$,

$$\boxed{\epsilon(p,k) = 1 - \sum_\alpha \frac{\omega_{p\alpha}^2}{n_\alpha k^2} \int \frac{f'_{0\alpha}(v_x)}{v_x - i\frac{p}{k}} \mathrm{d}v_x,} \tag{2.31}$$

where we have introduced the plasma frequency satisfying $\omega_{p\alpha}^2 = q_\alpha^2 n_\alpha/(\epsilon_0 m_\alpha)$.

The integral in the dielectric function is defined for $\mathrm{Re}(p) > \sigma$, and thus guaranteed to be defined for at least some $\mathrm{Re}(p) > 0$. The integration path crosses a pole when $\mathrm{Re}(p) = 0$. Moving p around can be seen as deforming the curve relative to p, and thus we will cross a pole if we where to deform it past $p = 0$. We must therefore add the residue that we otherwise would miss (Landau, 1946). Recalling the residue theorem, we have the following definition of the integral

$$\int \frac{f'_{0\alpha}(v_x)}{v_x - i\frac{p}{k}} \mathrm{d}v_x = \begin{cases} \displaystyle\int \frac{f'_{0\alpha}(v_x)}{v_x - i\frac{p}{k}} \mathrm{d}v_x, \quad \mathrm{Re}(p) > 0 & \text{(2.32a)} \\ \pi i f'_{0\alpha}\left(\frac{ip}{k}\right) + \mathcal{P}\displaystyle\int \frac{f'_{0\alpha}(v_x)}{v_x - i\frac{p}{k}} \mathrm{d}v_x, \quad \mathrm{Re}(p) = 0 & \text{(2.32b)} \\ 2\pi i f'_{0\alpha}\left(\frac{ip}{k}\right) + \displaystyle\int \frac{f'_{0\alpha}(v_x)}{v_x - i\frac{p}{k}} \mathrm{d}v_x, \quad \mathrm{Re}(p) < 0. & \text{(2.32c)} \end{cases}$$

To obtain the time evolution of the electrostatic potential, we must transform back to $\phi_{\boldsymbol{k}}$ from $\hat{\phi}_{\boldsymbol{k}}$ by inverse Laplace transforming

$$\phi_{\boldsymbol{k}} = \mathcal{L}^{-1}\{\hat{\phi}_{\boldsymbol{k}}\} = \frac{1}{2\pi i} \int_{-i\infty+\sigma}^{i\infty+\sigma} \hat{\phi}_{\boldsymbol{k}} \exp(pt) \mathrm{d}p. \tag{2.33}$$

By analytically continuing $\hat{\phi}_{\boldsymbol{k}}$, we can deform the integral path by taking $\mathrm{Re}(p) \to -\infty$, which will eventually enclose all poles of $\hat{\phi}_{\boldsymbol{k}}$. The deformed integration path is not changed topologically, as we close it in $\pm i\infty$, or in other words, on the top of the Riemann sphere. Using the residue theorem, we, by eq. (2.33), obtain that

$$\phi_{\boldsymbol{k}} = \sum_i c_i \exp(p_i t), \tag{2.34}$$

where the sum goes over all poles of $\hat{\phi}_{\boldsymbol{k}}$. Contributions will only be from poles as the integral over the curve goes to zero as $\exp(pt)$ (as we took $\mathrm{Re}(p) \to -\infty$). The coefficients c_i depend on the initial perturbation $g_{\boldsymbol{k}\alpha}$. As we noted before, $\hat{\phi}_{\boldsymbol{k}}$ is

analytical everywhere except when $\epsilon(p,k) = 0$. We can therefore look for zeros of $\epsilon(p,k)$ and say something about how perturbations will evolve in time. Positive real part of zeros of $\epsilon(p,k)$ in p yields an exponential growth of the potential, so called *inverse Landau damping*, whilst negative real part yields exponential decay of the potential, so called *Landau damping*. We are interested in these zeros as they tell whether there are any unstable solutions for a given $\boldsymbol{k}$. In real plasma systems, practically there are always fluctuations at all wave numbers. This means that if there exist unstable wave numbers, they will grow exponentially to significant values, no matter how small the fluctuations are that they grow from. Generally, the wavenumber corresponding to the largest growth rate will dominate.

2.3 Weibel Instabilities

Here we will reproduce the derivation of the equations governing the Weibel instability. The derivation used here deviates slightly from that performed originally by Weibel (1959). In contrast to the electrostatic instabilities, the growing modes are perpendicular to the propagation direction, in other words, it is a transverse wave. However, the steps of the derivation are analogous to those of the electrostatic instabilities. We will mostly follow Davidson (1983) but without introducing a background magnetic field, as we do not intend to consider magnetized plasmas.

We start with the collisionless Vlasov equation,

$$\frac{\partial f_\alpha}{\partial t} + \boldsymbol{v} \cdot \frac{\partial f_\alpha}{\partial \boldsymbol{x}} + \frac{q_\alpha}{m_\alpha}(\boldsymbol{E} + \boldsymbol{v} \times \boldsymbol{B}) \cdot \frac{\partial f_\alpha}{\partial \boldsymbol{v}} = 0, \tag{2.35}$$

which is the same as eq. (2.4) with the collision term neglected. It is convenient to move to Fourier space. The perturbations correspond to non-zero $\boldsymbol{k}$ and are assumed to be small, which yield

$$\frac{\partial f_{\boldsymbol{k}\alpha}}{\partial t} + \boldsymbol{v} \cdot i\boldsymbol{k} f_{\boldsymbol{k}\alpha} + \frac{q_\alpha}{m_\alpha}(\boldsymbol{E}_{\boldsymbol{k}} + \boldsymbol{v} \times \boldsymbol{B}_{\boldsymbol{k}}) \cdot \frac{\partial f_{0\alpha}}{\partial \boldsymbol{v}} = 0, \tag{2.36}$$

where we neglected second order terms. To eliminate the time derivative, we will again use the Laplace transform $\mathcal{L}$ to the dual time variable p, defined by eq. (2.21), and its inverse defined by eq. (2.22). We will again denote transformed variables with a hat. By Laplace transforming eq. (2.36) we obtain

$$p\hat{f}_{\boldsymbol{k}\alpha} + \boldsymbol{v} \cdot i\boldsymbol{k}\hat{f}_{\boldsymbol{k}\alpha} + \frac{q_\alpha}{m_\alpha}(\hat{\boldsymbol{E}}_{\boldsymbol{k}} + \boldsymbol{v} \times \hat{\boldsymbol{B}}_{\boldsymbol{k}}) \cdot \frac{\partial f_{0\alpha}}{\partial \boldsymbol{v}} = \text{init}, \tag{2.37}$$

and solving for $\hat{f}_{\boldsymbol{k}\alpha}$ yields

$$\hat{f}_{\boldsymbol{k}\alpha} = \text{init} - \frac{1}{\mathrm{p} + \boldsymbol{v} \cdot \mathrm{i}\boldsymbol{k}} \frac{\mathrm{q}_\alpha}{\mathrm{m}_\alpha}(\hat{\boldsymbol{E}}_{\boldsymbol{k}} + \boldsymbol{v} \times \hat{\boldsymbol{B}}_{\boldsymbol{k}}) \cdot \frac{\partial \mathrm{f}_{0\alpha}}{\partial \boldsymbol{v}}, \tag{2.38}$$

where we have gathered terms from the initial perturbation as "init".

To close the equations we will use Maxwell's equations. The equations needed are Ampère's law and Faraday's law. We Fourier transform these equations in the spatial variable to $\boldsymbol{k}$ and Laplace transform in time to p. The Fourier transform is denoted by a $\boldsymbol{k}$ index and the Laplace transform by a hat. By ignoring exactly what the initial perturbations are (as these contribute to the initial coefficient and not the growth rate), we obtain

$$\boldsymbol{\nabla} \times \boldsymbol{E} = -\frac{\partial \boldsymbol{B}}{\partial t} \qquad \Rightarrow i\boldsymbol{k} \times \hat{\boldsymbol{E}}_{\boldsymbol{k}} = -p\hat{\boldsymbol{B}}_{\boldsymbol{k}} + \text{init} \tag{2.39}$$

$$\boldsymbol{\nabla} \times \boldsymbol{B} = \mu_0\left(\boldsymbol{J} + \epsilon_0 \frac{\partial \boldsymbol{E}}{\partial t}\right) \Rightarrow i\boldsymbol{k} \times \hat{\boldsymbol{B}}_{\boldsymbol{k}} = \mu_0\left(\hat{\boldsymbol{J}}_{\boldsymbol{k}} + \epsilon_0 p\hat{\boldsymbol{E}}_{\boldsymbol{k}}\right) + \text{init} \tag{2.40}$$

where "init" incorporates the initial perturbations. The current can be expressed using the distribution function as

$$\begin{aligned} \hat{\boldsymbol{J}}_{\boldsymbol{k}} &= \sum_\alpha q_\alpha \iiint \boldsymbol{v} \hat{f}_{\boldsymbol{k}\alpha} \mathrm{d}^3 v \\ &= \sum_\alpha \frac{\omega_{p\alpha}^2 \varepsilon_0}{n_\alpha} \iiint \boldsymbol{v} \frac{-1}{p + \boldsymbol{v} \cdot i\boldsymbol{k}} (\hat{\boldsymbol{E}}_{\boldsymbol{k}} + \boldsymbol{v} \times \hat{\boldsymbol{B}}_{\boldsymbol{k}}) \cdot \frac{\partial f_{0\alpha}}{\partial \boldsymbol{v}} \mathrm{d}^3 v + \text{init}, \end{aligned} \tag{2.41}$$

where we used eq. (2.38) to express the distribution function, and we have also noted that $\omega_{p\alpha}^2 = n_\alpha q_\alpha^2/(m_\alpha \varepsilon_0)$.

Let us now align the z axis with the propagation direction, $\boldsymbol{k} = (0, 0, k)$ and look for transverse wave solutions. Align the x-axis with the perturbation direction of the electric wave, i.e. $\hat{\boldsymbol{E}}_{\boldsymbol{k}} = (\hat{E}_k, 0, 0)$. Faraday's law then becomes $\hat{\boldsymbol{B}}_{\boldsymbol{k}} = (0, -ik\hat{E}_k/p, 0) + \text{init}$, and the l.h.s. of Ampère's law is $i\boldsymbol{k} \times \hat{\boldsymbol{B}}_{\boldsymbol{k}} = (-k^2\hat{E}_k/p, 0, 0)$. By eliminating the magnetic field in favor of the electric field, the Lorentz force acting on the equilibrium distribution can be expressed as

$$(\hat{\boldsymbol{E}}_{\boldsymbol{k}} + \boldsymbol{v} \times \hat{\boldsymbol{B}}_{\boldsymbol{k}}) \cdot \frac{\partial f_{0\alpha}}{\partial \boldsymbol{v}} = \hat{E}_k \left[\frac{\partial f_{0\alpha}}{\partial v_x} + \frac{-ik}{p}\left(v_x \frac{\partial f_{0\alpha}}{\partial v_z} - v_z \frac{\partial f_{0\alpha}}{\partial v_x}\right)\right]. \tag{2.42}$$

We will now put it all together in Ampère's law eq. (2.40). The x component of Ampère's law reads

$$\left[-p^2 - c^2k^2 + \sum_\alpha \frac{\omega_{p\alpha}^2}{n_\alpha} \iiint \left(v_x \frac{\partial f_{0\alpha}}{\partial v_x} - \frac{ikv_x^2}{p + ikv_z} \frac{\partial f_{0\alpha}}{\partial v_z}\right) \mathrm{d}^3 v\right] \hat{E}_k = \text{init}, \tag{2.43}$$

where we noted that $\mu_0 \varepsilon_0 = 1/c^2$. The term in the integrand containing $\partial f_{0\alpha}/\partial v_x$ can be evaluated through integration by parts, and it yields $-n_\alpha$. This results in our final expression:

$$\left(-p^2 - c^2k^2 - \sum_\alpha \omega_{p\alpha}^2 - \sum_\alpha \frac{\omega_{p\alpha}^2}{n_\alpha} \iiint \frac{v_x^2}{v_z - \frac{ip}{k}} \frac{\partial f_{0\alpha}}{\partial v_z} \mathrm{d}^3 v\right) \hat{E}_k = \text{init}. \tag{2.44}$$

By the same argument as for the electrostatic case[2], the roots p_i of the factor in front of $\hat{E}_k$ yield electric-field terms of the form $\exp(p_i t)$. Using this observation, we arrive at the xx component of the dielectric tensor, that is, the effect of E_x on the electric displacement in the x direction,

$$\boxed{\epsilon_{xx} = -p^2 - c^2k^2 - \sum_\alpha \omega_{p\alpha}^2 - \sum_\alpha \frac{\omega_{p\alpha}^2}{n_\alpha} \iiint \frac{v_x^2}{v_z - \frac{ip}{k}} \frac{\partial f_{0\alpha}}{\partial v_z} \mathrm{d}^3 v.} \tag{2.45}$$

Note that for $ck \gg \omega_{p\alpha}$, we recover the vacuum dispersion relation $\omega^2 - k^2c^2 = 0$, where we used $p = -i\omega$ such that a real ω yield purely oscillating waves.

A more careful analysis of the dielectric tensor is done by Davidson (1983), where he lets the origin of the velocity coordinate system be at the average particle velocities in the x and y direction. This is done because then only diagonal elements to the dielectric tensor will be nonzero. The ϵ_{zz} is identical to the electrostatic dielectric function we derived in the previous section, and the ϵ_{yy} is symmetric to ϵ_{xx} in the sense that v_x is replaced by v_y. The dispersion relation is given by $\det\{\epsilon\} = \epsilon_{xx}\epsilon_{yy}\epsilon_{zz} = 0$.

2.3.1 Separable Distribution Functions in Velocity Space

We can consider the case when the distribution function has a separable v_z dependence. Then we can do the integrals separately, and the integral over v_x and v_y yield $\langle v_x^2 \rangle_\alpha^{\text{part}}$, and we arrive at

$$\boxed{\epsilon_{xx} = -p^2 - c^2k^2 - \sum_\alpha \omega_{p\alpha}^2 - \sum_\alpha \frac{\omega_{p\alpha}^2}{n_\alpha} \left\langle v_x^2 \right\rangle_\alpha^{\text{part}} \int \frac{f'_{0\alpha}(v_z)}{v_z - \frac{ip}{k}} \mathrm{d}v_z,} \tag{2.46}$$

where $f_{0\alpha}(v_z)$ is the marginal distribution in v_z and $f'_{0\alpha}(v_z)$ its derivative. If now the distribution in v_z is a Maxwellian, then we can express the dispersion relation in terms of the plasma dispersion function, Z, defined as

$$Z(\zeta) = \frac{1}{\sqrt{\pi}} \int_{-\infty}^{\infty} \frac{\exp(-u^2)}{u - \zeta} \mathrm{d}u, \tag{2.47}$$

where the integral is performed according to Landau's prescription (see eq. (2.32)). The dispersion relation when the distribution in the z direction is a Maxwellian becomes

$$\boxed{\epsilon_{xx} = -p^2 - c^2k^2 - \sum_\alpha \omega_{p\alpha}^2 - \sum_\alpha \omega_{p\alpha}^2 \frac{\langle v_x^2 \rangle_\alpha^{\text{part}}}{2 \langle v_z^2 \rangle_\alpha^{\text{part}}} Z'(\zeta_\alpha),} \tag{2.48}$$

[2]The argument starts at eq. (2.33).

where $\zeta_\alpha = ip/(k\sqrt{2\left\langle v_z^2\right\rangle_\alpha^{\text{part}}})$, and $Z'(\zeta) = -2(1+\zeta Z(\zeta))$ is the derivative of the plasma dispersion function w.r.t ζ.

2.4 Collisions in Plasmas

Here we will give a very brief outlook on Coulomb collisions in plasmas. We will start by the derivation for the deflection angle in Rutherford scattering. Then we will give a simple model of the accumulation of many small angle scattering events, and shortly discuss other models.

Consider an electron approaching an ion with speed v_0, and with *impact parameter* b. The impact parameter is defined as the smallest distance of approach that would occur if no forces act between the particles. As the ion mass is much larger than the electron mass, we may approximate the ion as stationary. Due to conservation of energy, the outgoing speed must also be v_0, and conservation of angular momentum yields that the final orthogonal distance must also be b. In light of this symmetry, introduce the canonical radial coordinates (r, ϕ), as shown in fig. 2.1, with their origin at the ion's position, and align the y-axis with the direction of the final change in momentum.

In this coordinate system, the Coulomb force is at all times directed in the radial direction, and thus the angular momentum is conserved. The initial angular momentum is $-m_\mathrm{e} v_0 b$. If scattered an angle 2θ, the change in momentum is $\Delta p_y = -2v_0 m_\mathrm{e}\sin(\theta)$. The scattering angle yields the boundary conditions on ϕ. The force directed towards the final change in momentum is

$$F_y = -\frac{Ze^2}{4\pi\epsilon_0 r^2}\sin(\phi), \tag{2.49}$$

where Ze is the ion charge. The impulse from this force is

$$I_y = \int_{-\infty}^{\infty} F_y \mathrm{d}t. \tag{2.50}$$

Now note that $r^2\,\mathrm{d}\phi/\mathrm{d}t = -bv_0$ is the angular momentum (apart from the constant mass factor) and is conserved. Thus the impulse is

$$I_y = -\int_{-\infty}^{\infty} \frac{Ze^2}{4\pi\epsilon_0 r^2}\sin(\phi)\mathrm{d}t = \frac{Ze^2}{4\pi\epsilon_0 b v_0}\int_{-\infty}^{\infty}\sin(\phi)\frac{\mathrm{d}\phi}{\mathrm{d}t}\mathrm{d}t. \tag{2.51}$$

The indefinite integral is just $-\cos(\phi)$, and the limits are $\phi = \pi + \theta$ and $\phi = -\theta$, which yields

$$I_y = -\frac{Ze^2}{2\pi\epsilon_0 b v_0}\cos(\theta). \tag{2.52}$$

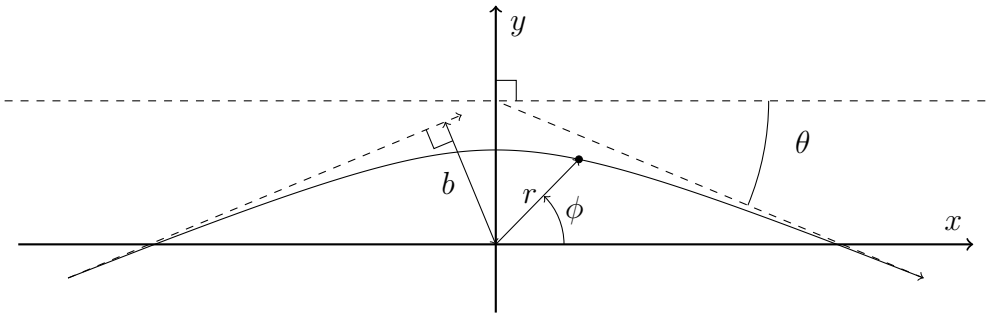

Figure 2.1: The path of an electron colliding with an ion in the coordinate system used here in describing the kinematics of charged particle collisions. We have defined the y-axis to be the symmetry axis, and given the particle a positive speed in the x-direction. From these Cartesian coordinates, the radial coordinates (r, ϕ) are defined. The electron starts at infinity with an angle $\phi = \pi + \theta$, impact parameter b and speed v_0. Symmetry implies that the electron will obtain the angle $\phi = -\theta$ after passing the ion (located at the origin), and thus scattered at an angle 2θ.

Equating this to the change in momentum we obtain

$$\tan(\theta) = \frac{Ze^2}{4\pi\epsilon_0 b m_\mathrm{e} v_0^2}. \tag{2.53}$$

By using the center-of-mass coordinate system instead, the resulting expression for half the scattering angle can be expressed as

$$\tan(\theta) = \frac{Ze^2}{4\pi\epsilon_0 \mu b v_0^2}, \tag{2.54}$$

where μ is the reduced mass,

$$\mu = \frac{m_\alpha m_{\alpha'}}{m_\alpha + m_{\alpha'}}, \tag{2.55}$$

and m_α and $m_{\alpha'}$ are the masses of the colliding particles.

Several of these scattering events add up to a significant scattering angle. For small angles, $\tan(\theta) \approx \theta$. In this limit, the diffusion of the velocity is proportional to θ^2. For small angle collisions, we must consider $2\theta < 1$, which in turn means $b > b_\mathrm{min}$, where b_min is the radius such that $2\theta = 1$, and coincides with the closest approach in a head-on collision between particles with the same kind of charge. As electric fields in a plasma are shielded on length scales larger than λ_D, we consider the case when $b < \lambda_D$.

An annular beam of radius b and width db with density n, speed v_0 would, during a time τ, undergo an accumulated scattering angle of $n\tau v_0 \theta^2 2\pi b \mathrm{d}b$. We may write the total scattering angle from such small-angle scattering events as

$$\Delta\theta_{\mathrm{tot}} = n\tau v_0 \int_{b_{\min}}^{\lambda_{\mathrm{D}}} \theta^2 2\pi b \mathrm{d}b = \frac{Z^2 e^4}{4\pi^2 \epsilon_0^2 m_{\mathrm{e}}^2 v_0^3} 2\pi\tau n \ln\left(\frac{\lambda_{\mathrm{D}}}{b_{\min}}\right). \tag{2.56}$$

We define the collision frequency as $\nu = (2\pi\tau)^{-1}$ such that $\Delta\theta_{\mathrm{tot}} = 1$, and introduce the quantity $\ln\Lambda = \ln(\lambda_{\mathrm{D}}/b_{\min})$. Consider electron–ion collisions, and let the characteristic relative speed be the electron thermal speed, $v_0 = v_{\mathrm{th}}$. Then we obtain the characteristic electron–ion collision frequency

$$\nu_{ei} = \frac{Z^2 e^4}{4\pi^2 \epsilon_0^2 m_{\mathrm{e}}^2 v_{\mathrm{th}}^3} n_{\mathrm{i}} \ln\Lambda, \tag{2.57}$$

where n_i is the ion density.

We call $\ln\Lambda$ the *Coulomb logarithm*, that in the plasmas of interest here is larger than unity. If $\ln\Lambda$ is larger than unity, then small angle scatterings dominate. However, in dense plasmas, $\ln\Lambda$ can be of order unity, then large angle collisions become important. In addition, in high density plasmas, many particle interactions and quantum effects become important. Moreover, very rare collisions can be important, for example in electrostatic shocks (Sundström *et al.*, 2019). There are much more elaborate models which takes these effects into account.

The collisions will gradually increase the entropy, and eventually drive any distribution function towards a Maxwell distribution[3]. A simple collision model is the Krook model (Bhatnagar, Gross & Krook, 1954). Then the collision operator is given by

$$C\{f\} = -\nu(f - f_{\mathrm{R}}), \tag{2.58}$$

where f is the distribution function, ν some collision frequency and f_{R} the distribution to which f wants to relax.

The isotropization caused by collisions will naturally compete with instabilities driven by anisotropies. Intuitively, collisions will lower the growth rate of an instability. In the case where the electron distribution function is a Maxwell distribution in all directions, but has a different width in one of the directions, that is, it has a temperature anisotropy, it is called a *bi-Maxwellian*. We define the temperatures $T_{\parallel} = m_{\mathrm{e}} \langle v_z^2 \rangle_{\mathrm{e}}^{\mathrm{fluid}}$ and $T_{\perp} = m_{\mathrm{e}} \langle v_x^2 \rangle_{\mathrm{e}}^{\mathrm{fluid}} = m_{\mathrm{e}} \left\langle v_y^2 \right\rangle_{\mathrm{e}}^{\mathrm{fluid}}$. Wallace *et al.* (1987) uses the Krook model to analytically find the effect of collisions on

[3]More generally the Maxwell-Jüttner distribution in the relativistic limit.

the Weibel instability in the case of a bi-Maxwellian distribution. He finds that the corrected growth rate γ^{C} can be expressed as

$$\gamma^{\mathrm{C}} = \gamma - \left(1 - \frac{T_{\parallel}}{T_{\perp}}\right)\nu, \tag{2.59}$$

where γ is the collisionless growth rate, and here the collision frequency is defined as

$$\nu = \frac{e^2\omega_{\mathrm{pe}}^2\sqrt{m_e}}{4\pi\epsilon_0 T_{\parallel}^{3/2}} \log\left(\frac{1.166 T_{\parallel}}{2\hbar\omega_{\mathrm{pe}}}\right). \tag{2.60}$$

Here $\hbar$ is the reduced Planck's constant. We see that collisions lower the Weibel growth rate, confirming our intuition.

2.5 PIC Simulations

In this section, we will give a brief introduction to the particle-in-cell (PIC) approach to numerical, kinetic modeling of plasmas, which is a particle-based method. Since the number of particles in any physically relevant plasma system is so large that following them individually would be numerically infeasible, so called macro-particles are introduced, each representing many particles. These macro-particles are evolved in time, as if they where ordinary particles obeying Newton's and Maxwell's equations. Evolving particles in both location and momentum is referred to as *pushing*.

The PIC loop consists of pushing the macro-particles using the Lorentz force. Then the charge and current densities are interpolated onto the electromagnetic grid. With these interpolated charge and current densities, Maxwell's equations are solved. The new fields are interpolated to the particle positions, and the loop starts over.

We can also view the macro-particles as discrete volume elements in phase space. The interpolation of the macro-particles onto the electromagnetic grid is what causes them have a volume in phase space. Therefore, we do not simulate the evolution of a phase-space volume, even though the particles are given a finite width. A schematic picture of this is presented in fig. 2.2, where the trajectory of macro-particle A is shown in real space. In this figure, for simplicity, the particle is given a shape of a rectangle, and its density is spread evenly over this rectangle. When solving Maxwell's equations, their integral form is used, and A deposits its contribution to the overall charge and current densities through how much its rectangle is intersecting with any grid cell in the discretization grid for the Maxwell's equations. The shape of the spread of A in phase space is given by the interpolation scheme used, where the rectangle is one possible choice.

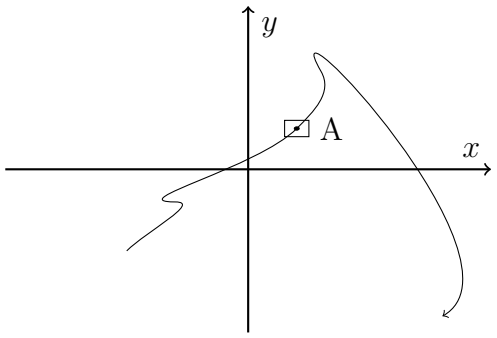

Figure 2.2: A hypothetical path of a particle A. The particle moves along its trajectory in real space. The rectangle symbolizes the extent of the particle A in real space. An equal point of view is that we simulate the phase-space volume around A. At each time step, the macro-particle deposits its charge and current density contribution to the electromagnetic grid through some interpolation method. It is this interpolation that defines the spatial extent of the macro-particle.

There are several different possible numerical implementations to achieve a PIC approach. A common way is to use a so called extended leapfrog algorithm to push the particles. The leapfrog algorithm updates the positions of the particles half a time step, then updates their velocities a full time step, and finally updates their positions the final half of the time step. The procedure is then repeated. The extended leapfrog algorithm was introduced by Boris (1970), and is commonly referred to as the Boris pusher. The basic concept is to use the leapfrog scheme for the electric field part, and for the magnetic field rotate the velocity vector with an angle corresponding to its gyro-motion. It is also common to discretize the electromagnetic fields on a Yee mesh (Yee, 1966). Then the locations of where the electric and magnetic fields are evaluated are shifted half a grid cell from each other. It is particularly useful when considering the integral form of Maxwell's equations. Using Stokes' theorem, the integral of the curl of the magnetic field over a cell surface is the line integral along the edges of that surface, which reduces to a sum of the magnetic field values, as these are evaluated in the middle of the edges of a cell. The volume integral over the divergence of the electric field over the cell is by Gauss' theorem a surface integral over the cell boundary, which reduces to a sum of all electric fields at the faces of the cell.

In fig. 2.3, the Yee mesh is illustrated. Blue vectors correspond to the electric field and red vectors to the magnetic field. The total flux of the electric field out from this cell is the sum over all electric field values which are evaluated at the center of the faces of the cell. The total rotation of the magnetic field for any face of the cell is the sum over all magnetic field components at the edges of that

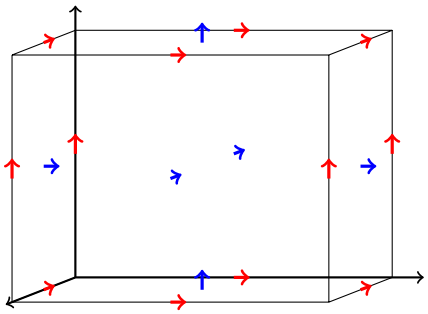

Figure 2.3: The Yee mesh. Electric fields shown by the blue arrows are evaluated on the center of the faces. These contribute to a flux in and out of the cell, corresponding to the charge density by Gauss's law. The magnetic fields shown in red are evaluated on the center of the edges. For each surface they contribute to a rotation, coupled to the current density by Ampere's law. In turn, by shifting the cell half a step across a cell diagonal, it will show a similar picture, but instead with the electric fields evaluated on the edges and magnetic fields on the faces. This then couples the rotation of the electric field with the magnetic field through Faraday's law. The magnetic field values on the faces are then used in Gauss's law for magnetism.

face. By moving the cell half a step in each direction (diagonally), we transpose the electric fields to the edges and the magnetic fields to the faces. It is now possible to advance the magnetic field with Faraday's induction law, using the same concept with the edges and faces to calculate flux.

We sometimes considered collisions in our simulations. Then, we used the model by Nanbu (1997). They consider each small random velocity change individually and calculate the distribution of the scattering angle after N successive scattering events. This approach is extended with weighting schemes in Nanbu & Yonemura (1998) to be suitable for PIC, and got further improved by Perez *et al.* (2012). Since they consider each binary scattering event individually, eq. (2.54) still holds to express the scattering of a single small angle collision. Especially when $\ln \Lambda$ is not large, the choice of collision model can be of importance, see for example the discussion in section 3.2 in Sundström *et al.* (2020). We found good agreement with our simulations and previous analytical results, and did therefore not test other collisional models.

In this thesis, the Smilei (Derouillat *et al.*, 2018) PIC code is used. Particularly, we will use the implemented Yee mesh and the Boris pusher. We will use an interpolation order of four when the macro-particles are interpolated to configuration space (and their velocities are point velocities). The boundary conditions in configuration space are periodic boundary conditions. It is possible to simulate one to three spatial dimensions. When simulating N spatial dimensions and M

momentum dimensions, it is referred to as a NDMP simulation. For example, a 1D3P simulation uses one space dimension and three momentum dimensions. Since momentum space is not represented by a mesh, unlike the spatial dimensions, most PIC simulations retain all three momentum dimensions, even at lower spatial dimensionality.

Chapter 3

Electrostatic Stability of the Ring Distribution

In this chapter, we will first give a summary of our analytical derivation of the electrostatic stability of the ring distribution. Complementary material to the derivation can be found in appendix A. Then, we will show results from PIC simulations of partially open ring distributions. In other words, the distributions have gaps, and are not 2D-isotropic. We will find that these can either close themselves to ring distributions, or collapse to a more Maxwell-like distribution.

3.1 Electrostatic Stability of the Ring Distribution

In this section, we will give a summary of the results from our analytical derivation of the electrostatic stability of ring distributions. Explanatory steps between equations are found in appendix A.

3.1.1 Dielectric Function for a Cold Ring

We will start with a cold (no thermal broadening) ring distribution. Using a density plot, we visualize the distribution function in $v_x v_y$-space in fig. 3.1a. The marginal distribution in v_x is visualized in fig. 3.1b. Mathematically, we can write down the joint distribution function in polar coordinates as

$$f(v_r, \theta) = \frac{n_\mathrm{e}}{2\pi v_\mathrm{m}} \delta(v_r - v_\mathrm{m}), \tag{3.1}$$

where δ is the Dirac delta distribution, v_r is the speed in the $v_x v_y$-plane, θ the polar angle, v_m is the speed determining the radius of the ring that we shall refer to as the *mode speed*, and n_e is the density of electrons.

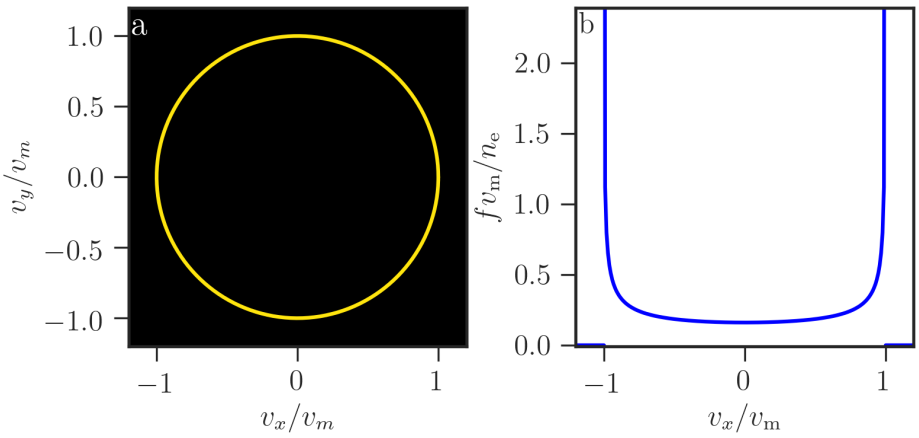

Figure 3.1: The cold ring electron distribution in panel (a) and its marginal distribution in panel (b). In panel (a), a density plot is used to visualize the distribution function. The distribution is infinitesimally narrow. We observe a divergence in the marginal distribution as $|v_x| \to v_\mathrm{m}$ (panel (b)). This divergence is not present in *distribution representations* of the delta function.

We use eq. (2.31) to express the dielectric function. To evaluate the integral, we consider the case when $\mathrm{Re}(p) > 0$. In this case, the integral is defined by eq. (2.32a). We can express the marginal distribution as

$$f_x(v_x) = \begin{cases} \frac{n_\mathrm{e}}{\pi\sqrt{v_\mathrm{m}^2 - v_x^2}}, & \text{if } |v_x| < v_\mathrm{m} \\ 0, & \text{if } |v_x| > v_\mathrm{m}. \end{cases} \tag{3.2}$$

We be evaluating the integral in eq. (2.31) to obtain the dielectric function. A slightly more general form of the dielectric function than the one obtained in this section will later be used to show the electrostatic stability. To compact the notation, we transform to the dimensionless variables $u = v_x/v_\mathrm{m}$, $\alpha = p/(v_\mathrm{m}k)$ and $\beta = v_\mathrm{m}k/\omega_\mathrm{pe}$. In this notation, and by integrating by parts, we obtain

$$\frac{\omega_\mathrm{pe}^2}{k^2}\frac{1}{n_\mathrm{e}}\int_{-\infty}^{\infty}\frac{\frac{\mathrm{d}f_x}{\mathrm{d}v_x}}{v_x - ip/k}\mathrm{d}v_x = \beta^{-2}\frac{1}{\pi}\int_{-1}^{1}\frac{1}{\sqrt{1-u^2}}\frac{1}{(u-i\alpha)^2}\mathrm{d}u, \tag{3.3}$$

which is also what one obtains using the heat kernel representation of the delta distribution. This integral form is listed in Gradshteyn & Ryzhik (2007, sec. 2.252), and can be simplified by using the substitution $\xi = -i(u - i\alpha)^{-1}$. With this

substitution, it is possible to express the integral as

$$\begin{aligned}\beta^{-2}\frac{1}{\pi}\int_{-1}^{1}\frac{1}{\sqrt{1-u^2}}\frac{1}{(u-i\alpha)^2}\mathrm{d}u \\ = \beta^{-2}\frac{-i}{\pi\sqrt{1+\alpha^2}}\int_{u=-1}^{u=1}\frac{\alpha}{\sqrt{((1+\alpha^2)\xi-\alpha)^2+1}}\mathrm{d}\xi.\end{aligned} \tag{3.4}$$

By transforming according to $\eta = (1+\alpha^2)\xi - \alpha$, we obtain an integral on the form $(1+\eta^2)^{-1/2}$ which has the primitive function $\sinh(\eta)$,

$$\begin{aligned}\beta^{-2}\frac{-i}{\pi\sqrt{1+\alpha^2}}\int_{u=-1}^{u=1}\frac{\alpha}{\sqrt{((1+\alpha^2)\xi-\alpha)^2+1}}\mathrm{d}\xi \\ = \beta^{-2}\frac{-i\alpha}{\pi(1+\alpha^2)^{3/2}}\left[\sinh^{-1}(\eta)\right|_{u=-1}^{u=1}.\end{aligned} \tag{3.5}$$

One needs to be careful to check that the primitive function is analytical along the integration path, which is true in this case. Analyzing the limits yields that

$$\left[\sinh^{-1}(\eta)\right|_{u=-1}^{u=1} = -i\pi, \tag{3.6}$$

and after algebraic manipulations, we arrive to the dielectric function

$$\boxed{\epsilon(p,k) = 1 + \frac{\frac{p}{\omega_{\mathrm{pe}}}}{\left(\frac{v_{\mathrm{m}}^2k^2}{\omega_{\mathrm{pe}}^2} + \frac{p^2}{\omega_{\mathrm{pe}}^2}\right)^{3/2}}.} \tag{3.7}$$

Recall that the details of the calculation can be found in appendix A.

3.1.2 Dielectric Function for Warm Ring

Next, we would like to know how a finite thermal width affects the dielectric function. To obtain this expression, we first find a general expression for the integral in eq. (2.32a). By using the trick that any function can be expressed as a convolution between a delta distribution and itself, we can use our previous integration result to find that for any 2D-isotropic distribution $f(v_r,\theta) = f(v_r)$ we have

$$\boxed{-\frac{\omega_{\mathrm{pe}}^2}{k^2}\frac{1}{n_{\mathrm{e}}}\int_{-\infty}^{\infty}\frac{\frac{\mathrm{d}f_x(v_x)}{\mathrm{d}v_x}}{v_x - i\frac{p}{k}}\mathrm{d}v_x = \frac{1}{n_{\mathrm{e}}}\int_0^{\infty}f(v_r)\frac{\frac{p}{\omega_{\mathrm{pe}}}}{\left(\frac{v_r^2k^2}{\omega_{\mathrm{pe}}^2} + \frac{p^2}{\omega_{\mathrm{pe}}^2}\right)^{3/2}}v_r\mathrm{d}v_r.} \tag{3.8}$$

Here $f_x(v_x)$ is used to denote the marginal distribution of $f(v_r)$.

To obtain a ring shape with a width, we a use a rotated Maxwellian,

$$f(v_x, v_y) = N \exp\left(-\frac{\left(\sqrt{v_x^2 + v_y^2} - v_\mathrm{m}\right)^2}{v_d^2} \right), \tag{3.9}$$

where N is the normalization constant such that the distribution integrates to n_e, v_m is the speed at which the distribution function attains its maximum (the mode speed), and v_d corresponds to the thermal width of the distribution around the mode speed. The normalization constant is

$$N = \frac{n_\mathrm{e}}{2\pi} \left\{ \frac{v_d^2}{2} \exp\left(-\frac{v_\mathrm{m}^2}{v_d^2} \right) + \frac{v_\mathrm{m} v_d}{2} \sqrt{\pi} \left[1 + \operatorname{erf}\left(\frac{v_\mathrm{m}}{v_d} \right) \right] \right\}^{-1}. \tag{3.10}$$

By inspecting eq. (3.8), we note that the factor multiplying f has a primitive function in v_r given by

$$\chi(v_r) = \frac{\frac{p}{\omega_\mathrm{pe}}}{\sqrt{\frac{v_r^2 k^2}{\omega_\mathrm{pe}^2} + \frac{p^2}{\omega_\mathrm{pe}^2}}}, \tag{3.11}$$

up to a constant factor. Substituting to χ, we can express the integral for a rotated Maxwellian as,

$$\begin{aligned} &\frac{2\pi}{n_\mathrm{e}} \int_0^\infty f(v_r) \frac{\frac{p}{\omega_\mathrm{pe}}}{\left(\frac{v_r^2 k^2}{\omega_\mathrm{pe}^2} + \frac{p^2}{\omega_\mathrm{pe}^2} \right)^{3/2}} v_r \mathrm{d}v_r \\ &\quad = \frac{2\pi}{n_\mathrm{e}} \frac{\omega_\mathrm{pe}^2}{k^2} \int_0^1 N \exp\left(-\frac{\left(\frac{p}{k} \sqrt{\frac{1}{\chi^2} - 1} - v_\mathrm{m} \right)^2}{v_d^2} \right) \mathrm{d}\chi. \end{aligned} \tag{3.12}$$

For small v_d it is possible to Taylor expand the exponent in χ around its maximum. Expanding to second order yield an integral of a Gaussian, and extending the limits from $[0, 1]$ to $[-\infty, \infty]$, we can find an approximate form to the integral analytically. This is basically the saddle point method. It is found that

$$\begin{aligned} &\frac{2\pi}{n_\mathrm{e}} \frac{\omega_\mathrm{pe}^2}{k^2} \int_0^1 N \exp\left(-\frac{\left(\frac{p}{k} \sqrt{\frac{1}{\chi^2} - 1} - v_\mathrm{m} \right)^2}{v_d^2} \right) \mathrm{d}\chi \\ &\quad \approx \frac{2\pi^{3/2} N v_d v_\mathrm{m}}{n_\mathrm{e}} \frac{\frac{p}{\omega_\mathrm{pe}}}{\left(\frac{v_\mathrm{m}^2 k^2}{\omega_\mathrm{pe}^2} + \frac{p^2}{\omega_\mathrm{pe}^2} \right)^{3/2}}. \end{aligned} \tag{3.13}$$

This yields the dielectric function as

$$\boxed{\epsilon(p,k) \approx 1 + \frac{2\pi^{3/2} N v_d v_\mathrm{m}}{n_\mathrm{e}} \frac{\frac{p}{\omega_\mathrm{pe}}}{\left(\frac{v_\mathrm{m}^2 k^2}{\omega_\mathrm{pe}^2} + \frac{p^2}{\omega_\mathrm{pe}^2}\right)^{3/2}}.} \tag{3.14}$$

This is quite similar to the result from the cold ring. Note that when $v_d/v_m \to 0$, we recover the dielectric function from a cold ring.

3.1.3 Stability of Ring Distributions

We note that for both the cold ring and warm ring, the dielectric function is of the form

$$\epsilon_S(p,k) = 1 + S \frac{\frac{p}{\omega_\mathrm{pe}}}{\left(\frac{v_\mathrm{m}^2 k^2}{\omega_\mathrm{pe}^2} + \frac{p^2}{\omega_\mathrm{pe}^2}\right)^{3/2}}, \tag{3.15}$$

where $S > 0$ is some shape parameter. To show the inexistence of roots corresponding to growing modes, we will use Cauchy's argument principle in the fourth quadrant in p. The fourth quadrant in p corresponds to electric waves propagating in the positive x direction, and growing exponentially in magnitude. As the problem is symmetric to rotations around the z-axis, propagation direction can without loss of generality be chosen arbitrarily in the xy-plane. Cauchy's argument principle states that for a simple counter-clockwise oriented closed curve $\delta\Omega$,

$$Z - P = \frac{1}{2\pi i} \oint_{\delta\Omega} \frac{g'(z)}{g(z)} \mathrm{d}z, \tag{3.16}$$

where Z and P are the number of zeros and poles of g in Ω, respectively, g is a meromorphic function on Ω, and Ω the interior of $\delta\Omega$. This assumes that there are no poles or zeros on $\delta\Omega$. Now as $\int (g'/g)\mathrm{d}z = \log(g(z))$, we can evaluate the total infinitesimal changes in the argument of $g(z)$ to obtain the number of zeros minus the number of poles. If $g(z)$ is analytical inside Ω, then we can obtain the number of zeros by evaluating the change in argument. Note that the Nyquist method can be proved using this principle.

We use the normalized variables $\beta = v_\mathrm{m} k/\omega_\mathrm{pe}$ (as before) and $G = p/\omega_\mathrm{pe}$ to simplify our algebraic expressions. Physically, the real part of G is the normalized growth (decay) rate when it is positive (negative). The imaginary part of G is the corresponding normalized oscillation frequency. Roots of $\epsilon_S(p,k) = 0$ are given by

$$0 = (\beta^2 + G^2)\sqrt{\beta^2 + G^2} + SG =: h(G), \tag{3.17}$$

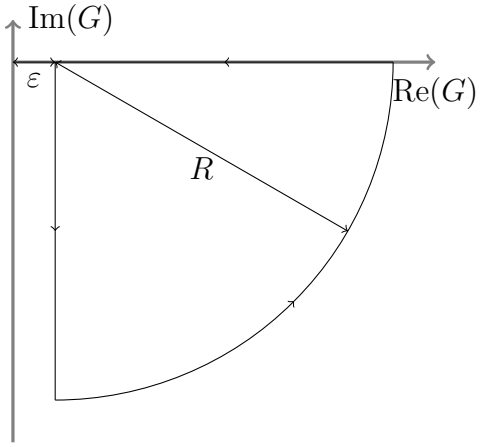

Figure 3.2: The curve $\delta\Omega_R$, used to find the argument variation of h. As R goes to infinity and ε to 0, the curve encloses the entire fourth quadrant.

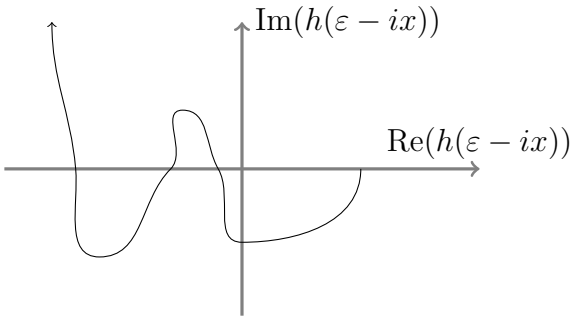

Figure 3.3: A schematic picture of the set $\{h(\varepsilon - ix) : x \in [0, R]\}$. We prove that it can only cut the negative real axis; the argument of h goes to $\pi/2$ when x approaches infinity, and is 0 when $x = 0$.

where we defined $h(G)$. The change in argument is calculated over the closed curve $\delta\Omega_R = [\varepsilon, \varepsilon - iR] \cup \delta\Omega_C \cup [R, \varepsilon]$, shown in fig. 3.2. Here $\delta\Omega_C$ is the quarter circular arc, shifted by ε to the right in the fourth quadrant in the complex plane. We can parameterize it as $\delta\Omega_C = \{z : z = \varepsilon + R\exp(i\theta), \quad \theta \in [-\pi/2, 0]\}$.

As $h(G)$ is holomorphic on the interior of $\delta\Omega_R$, the total change in its argument yields the number of roots times 2π. Note that a zero of $h(G)$ is a zero of ϵ_S and vice versa. The radius R will be taken to infinity and ε to zero to capture the entire fourth quadrant. The shift by ε is needed as the line segment given by $[0i, -iR]$ will cut 0 (implying that there might exist a purely complex root).

The change in argument for the curve given by $[R, \varepsilon]$ is 0, as for any real positive G the argument of h is 0. When R is sufficiently large, we have that $|h - G^3| < |G^3|$ on $\delta\Omega_C$. We can therefore use G^3 to find the change in argument of h on $\delta\Omega_C$, which yields $\frac{3}{2}\pi$.

For the $[\varepsilon, \varepsilon - iR]$ curve, we parameterize it with $G = \varepsilon - ix$, $x \in [0, R]$. Analyzing the argument of h at the end points yield that it starts at 0, since it is real and positive at $x = 0$. When $x \to \infty$, the argument goes to $\pi/2$ as the imaginary part diverges to $+\infty$, as x^3, whereas the real part diverges to $-\infty$, as $x^{3/2}$. The goal is to show that $h(\varepsilon - ix)$ only cuts the negative real axis. Then the change in argument is $-\frac{3}{2}\pi$, as we only cut the negative real axis and the curve departs from $(\beta^2 + \varepsilon^2)^{3/2} + S\varepsilon - i0$. A schematic picture of the curve is shown in fig. 3.3.

It is now left to show that $h(\varepsilon - ix)$ only cuts the negative real axis. As the imaginary part of $h(\varepsilon - ix)$ is always negative when $0 < x < \beta$, h does not cut

the real axis when $0 < x < \beta$. For $x \geq \beta$, we can consider the Taylor expansion in ε to find where $\mathrm{Im}(h) = 0$. It is not obvious that it is possible to Taylor expand to find where the imaginary part is zero. In appendix A.5, we use an explicit expression for the principal square root to show that it is possible, but it requires more algebra. We find that

$$h(\varepsilon - ix) = \varepsilon\Big(S - 3x\sqrt{x^2 - \beta^2}\Big) + i[(x^2 - \beta^2)\sqrt{x^2 - \beta^2} - Sx] + \mathcal{O}(\varepsilon^2). \quad (3.18)$$

Note that we have used $x > 0$ and $\varepsilon > 0$ to evaluate what sign to use for the principle branch of the square root. Solving $\mathrm{Im}(h) = 0$, we find that

$$Sx = (x^2 - \beta^2)^{3/2} + \mathcal{O}(\varepsilon^2). \quad (3.19)$$

We can rewrite the real part of h to match this expression,

$$\mathrm{Re}(h) = \frac{\varepsilon}{x}\sqrt{x^2 - \beta^2}\left(\frac{Sx}{\sqrt{x^2 - \beta^2}} - 3x^2\right) + \mathcal{O}(\varepsilon^2). \quad (3.20)$$

Using eq. (3.19) to evalute the term containing S, and then using the inequality $-x^2\sqrt{x^2 - \beta^2} \leq 0$, we find that

$$\mathrm{Re}(h) + \mathcal{O}(\varepsilon^2) = -\frac{\varepsilon}{x}\sqrt{x^2 - \beta^2}\Big(2x^2 - \beta^2\Big) \leq -\frac{\varepsilon}{x}\Big(x^2 - \beta^2\Big)^{3/2} = -\varepsilon S, \quad (3.21)$$

where we in the last equality again used eq. (3.19). This means that $\mathrm{Re}(h)$ is strictly negative for sufficiently small ϵ as both S and ε are strictly positive. Thus h only cuts the real axis at strictly negative real values, and the change in argument is $-\frac{3}{2}\pi$. All in all, the total change in argument is 0. As this is true for any sufficiently small $\varepsilon > 0$[1], we have no roots in the fourth quadrant.

We have arrived to the main result of this section, all distributions yielding a dielectric function that has the form of eq. (3.15) are linearly, electrostatically stable. These distributions include ring distributions of a small finite width and of zero width. It is known that 3D isotropic distributions are electrostatically stable, which can be proven by showing that the marginal distribution of a 3D isotropic distribution is decreasing monotonically in kinetic energy. We have found that a class of 2D isotropic distributions is also electrostatically stable, even though they have a clear non-monotonicity in kinetic energy, as seen in fig. 3.1b. The stability of the cold ring distribution is a strong indication that likely a much larger class of 2D-isotropic distributions, if not all, are stable. For these to be stable, it is sufficient to show that the integral will yield a dielectric function on the form eq. (3.15). Note that this concerns strictly the *electrostatic* stability; the ring distribution is unstable to the (electromagnetic) Weibel instability.

[1]It must be true for any $\varepsilon > 0$, although it is not what we have proven here.

3.2 PIC Simulations of Partially Open Rings

Since the ring is electrostatically, linearly stable, it is not expected to disintegrate in an electrostatic simulation. This is indeed what we observe, and thus, being of no additional interest, do not show these simulations here. In this section, we will instead present particle-in-cell (PIC) simulations that test how robust the ring distribution is to imperfections in its isotropy. We simulated several circular arc distributions. These distributions consist of two circular arcs opposite each other. The arcs were given the same radius, but with different angular span and thermal width, between different simulations. We first describe the setup used, and then discuss the results from our simulations. If the circular arc distribution is sufficiently close to a ring, it collapses to one.

3.2.1 Simulation Setup

The simulations are performed using the PIC code Smilei (Derouillat *et al.*, 2018), and done in 2D3P. All cases use a *mode speed* of $v_\mathrm{m} = 0.054c$, corresponding to kinetic energy of 750 eV. We normalize the time coordinate to ω_pe, and thus the value of the density will not appear explicitly.

In the cold case, all the electron macro-particles have the mode speed v_m, and are randomly distributed in polar angle in the $p_x p_y$-plane. For the 70 % closed cases, there are two gaps at opposing polar angles with a gap size of 15 % (54°), and for the 90 % cases, there are two gaps at opposing polar angles with a gap size of 5 % (18°). The initial distributions can be seen in panel (a) of figs. 3.4–3.7. For the warm distributions, the same setup was used, but we added a random Maxwellian term corresponding to a temperature of $T = 60\,\mathrm{eV}$ in both p_x and p_y. Mathematically, the initial velocities are

$$v_{x0} = v_\mathrm{m} \sin(\Theta) + \frac{v_\mathrm{th}}{\sqrt{2}} \mathcal{N}(0,1), \tag{3.22}$$

and

$$v_{y0} = v_\mathrm{m} \cos(\Theta) + \frac{v_\mathrm{th}}{\sqrt{2}} \mathcal{N}(0,1), \tag{3.23}$$

where $\mathcal{N}(0,1)$ is a normally distributed random variable with mean 0 and standard deviation 1, and Θ is a random variable uniformly distributed on $[\eta\pi, (1-\eta)\pi] \cup [(1+\eta)\pi, (2-\eta)\pi]$ where η is 0.15 for the 70 % closed case and 0.05 in the 90 % closed case. In the cold case, the $\mathcal{N}(0,1)$ term is removed. Note that in the warm case, the Maxwellian thermal broadening allows particles to obtain arbitrary angles, although it does not fully close the gaps. We initialize the third velocity direction to zero. The ions are placed randomly in space with zero velocity, and are not evolved.

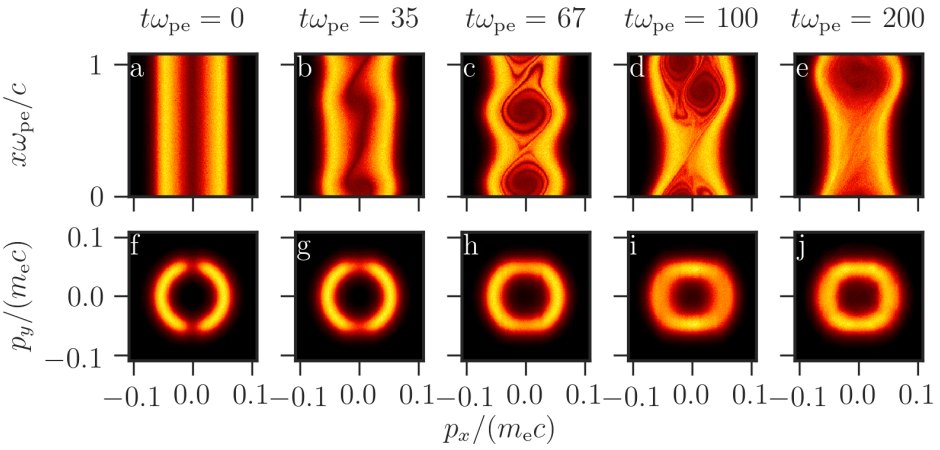

Figure 3.4: The marginal distribution function in xp_x-space in panels (a)–(e) (top row), and the marginal distribution in p_xp_y-space in panels (f)–(j) (bottom row). Time evolves when moving along each row. The initial distribution is a 90 % closed warm ring with its mode speed at $0.054c$ (corresponding to kinetic energy of 750 eV) and a width from a Maxwellian distribution with a temperature of 60 eV.

The simulation box size is $100\lambda_{\mathrm{D}} \times 100\lambda_{\mathrm{D}}$ (defined for $T = 60\,\mathrm{eV}$) and is split into 1024×1024 cells. The time step is approximately 64 % of the Courant-Friedrichs-Lewy (CFL) time and we simulate for a duration of $120\omega_{\mathrm{pe}}^{-1}$ for the cold particles and $200\omega_{\mathrm{pe}}^{-1}$ for the warm particles. Each cell contains on average 8 particles of each species, and the particles are randomly distributed in space with a uniform distribution.

3.2.2 Dynamics of Incomplete Ring Distributions

We find that when the circular arc distribution is sufficiently close to a ring, it collapses to one. We will present four cases: a 70 % closed cold ring, a 70 % closed warm ring, a 90 % closed cold ring, and a 90 % closed warm ring. The evolution of the 90 % closed warm and cold distributions are shown in fig. 3.4 and fig. 3.5, respectively. In figs. 3.6 and 3.7 the evolution of the 70 % closed warm/cold ring is shown. For all figs. 3.4–3.7, the top row shows the marginal distribution in p_xx-space, and the bottom row shows the marginal distribution in p_xp_y-space. The coloring is normalized to the maximum of the distribution at each specific time. Each column corresponds to a specific time. In all cases, except for the 70 % closed cold ring, the distribution tends to a ring distribution, seen in panels (j) of figs. 3.4–3.6. Instead, the 70 % closed cold ring tends to something which could be an intermediate step towards a Maxwellian, seen in fig. 3.7j.

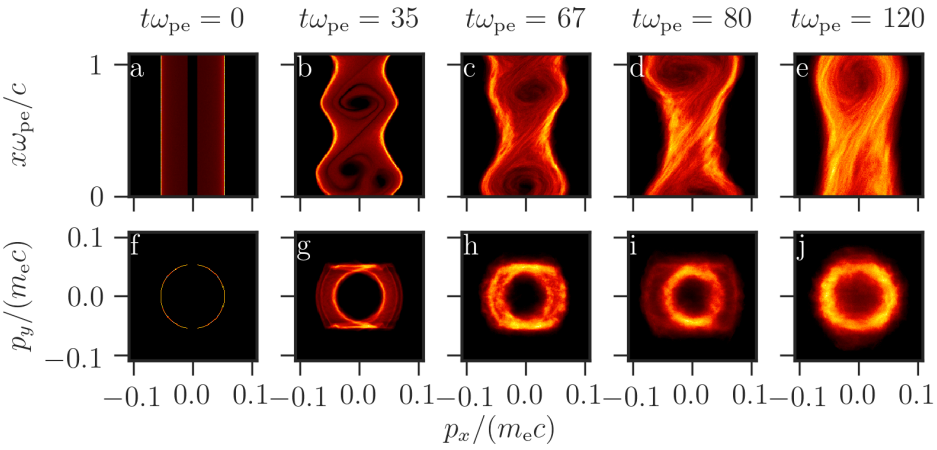

Figure 3.5: The marginal distribution function in xp_x-space in panels (a)–(e) (top row), and the marginal distribution in p_xp_y-space in panels (f)–(j) (bottom row). Time evolves when moving along each row. The initial distribution is a 90 % closed cold ring and with a constant speed of $0.054c$ (corresponding to kinetic energy of 750 eV).

In all cases, the instability produces phase-space signatures of a two-stream instability (TSI). Bernstein, Greene & Kruskal (1957) find that plasmas support non-linear (quasi-)steady state solutions, which we refer to, after the initials of these authors, as BGK modes. There are examples in the literature for BGK modes to form when the TSI reach a large amplitude. A certain class of BGK modes is reminiscent of a hole in phase space (similar to the structure seen in fig. 3.6e); these are called phase-space holes. Ghizzo *et al.* (1988) finds that such holes, initially generated on scales corresponding to the fastest growing wave number of the instability, tend to undergo coalescence to form larger phase-space holes. In the non-linear phase of the instability, these holes attract each other, and merge successively. Eventually, only one hole is left, and small wavelength structures are damped. This merging can be understood analytically by examining the eigenfunctions of the perturbations (Siminos, Bénisti & Gremillet, 2011).

We observe the creation and merging of phase-space holes in the top row of figs. 3.4–3.7. For all cases, except the 70 % warm case, successive merging events make the marginal p_xp_y-distribution more ring shaped (bottom row of figs. 3.4, 3.5 and 3.7) During a merge, the ring shape is disturbed. In the final time step, after all merges, the distribution is almost completely ring shaped (panel (j) of figs. 3.4–3.7). When we start with a complete ring distribution, we do not obtain any phase-space holes (not shown here).

Interestingly, even though we observe holes in the xp_x distributions, the p_xp_y

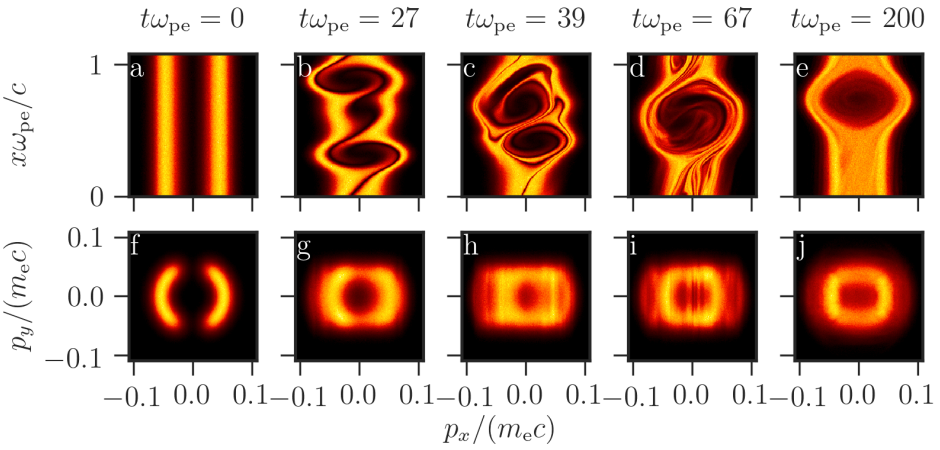

Figure 3.6: The marginal distribution function in xp_x-space in panels (a)–(e) (top row), and the marginal distribution in p_xp_y-space in panels (f)–(j) (bottom row). Time evolves when moving along each row. The initial distribution is a 70 % closed warm ring with its mode speed at $0.054c$ (corresponding to kinetic energy of 750 eV) and a width from a Maxwellian distribution with a temperature of 60 eV.

marginal distribution in the final time step is ring shaped. For the 90 % closed cases, the density profile in x tends to the average density after the instability phase. To show this, we compare the Fourier modes of the distribution $f_{\boldsymbol{k}e}$ with f_{0e} from eq. (2.14). The modes $f_{\boldsymbol{k}e}$ are the spatial fluctuations of the distribution. We can write the spatially averaged root mean square density fluctuation δn_{e} through

$$(\delta n_{\mathrm{e}})^2 \coloneqq \left\langle \left(\int f_e \mathrm{d}^3v - n_{\mathrm{e}} \right)^2 \right\rangle_x = \sum_{\boldsymbol{k}\neq 0} \int f_{\boldsymbol{k}e}(\boldsymbol{v}, t)\mathrm{d}^3v \int f_{-\boldsymbol{k}e}(\boldsymbol{v}', t)\mathrm{d}^3v'. \tag{3.24}$$

In fig. 3.8, $\delta n_{\mathrm{e}}/n_{\mathrm{e}}$ is plotted over time, using the l.h.s. of eq. (3.24)[2]. As we see, the density fluctuations rise initially due to the instability, but then later decay when the average velocity distribution becomes sufficiently isotropic (ring shaped) to become linearly stable. For all cases except the 70 % warm case, density fluctuations tend to small values over time. Instead, in the 70 % warm case, the density fluctuation seem to saturate. We expect from linear theory that small density fluctuations will eventually disappear through phase mixing and Landau damping. However, as we noted previously, there can be equilibrium distributions which are non-homogeneous in space (see for example eq. (2.12)). These distributions –

[2]We analytically perform the dy integral by approximating the y density fluctuations to be 0, due to numerical limitations on resolving the full 2D fluctuations.

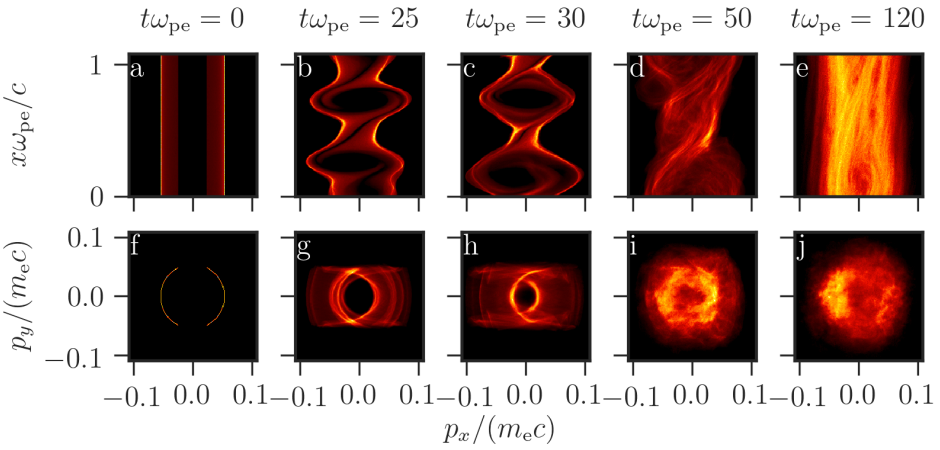

Figure 3.7: The marginal distribution function in xp_x-space in panels (a)–(e) (top row), and the marginal distribution in p_xp_y-space in panels (f)–(j) (bottom row). Time evolves when moving along each row. The initial distribution is a 70 % closed cold ring and with a constant speed of $0.054c$ (corresponding to kinetic energy of 750 eV).

the previously mentioned BGK modes – can be non-linearly stable. Although it is very interesting to know if the final distribution is a non-linear stable distribution or not, it is out of the scope of this thesis.

We also notice that the marginal p_y distribution changes much slower (than the marginal p_x distribution), seen best by the sharp flat edges in fig. 3.7g. This is due to that instabilities in p_y are much less prominent. When examining the xy-distribution, it is clear that there are almost no perturbations in the y-direction. This is expected, as the initial marginal distribution function in p_y is proportional to the one in fig. 3.1b, but zero at about $[-1.0v_{\mathrm{m}}, -0.9v_{\mathrm{m}}]$ and $[0.9v_{\mathrm{m}}, 1.0v_{\mathrm{m}}]$, which is much less like a two-stream and more like Maxwellian or a flat distribution.

A possible explanation why the distribution closes into a ring can be the minimization of free energy. Consider an electron with a fixed energy, and only moving in the xy-plane. Also consider the case where no large electrostatic potentials are present. Then the particle is constrained to be on the circle in v_xv_y-space (as the kinetic energy is approximately conserved). With this constraint the free energy is minimized by maximizing its entropy. The entropy is maximized when the particle is allowed to be anywhere on circle in phase space, corresponding to the distribution assuming a ring shape. For larger energy transfers in particle–wave interactions (more perturbed), one could imagine that the distribution changes more and instead reach the Maxwell distribution.

One limitation of these simulations is that a particle with $v_x = v_{\mathrm{m}} = 0.054c$,

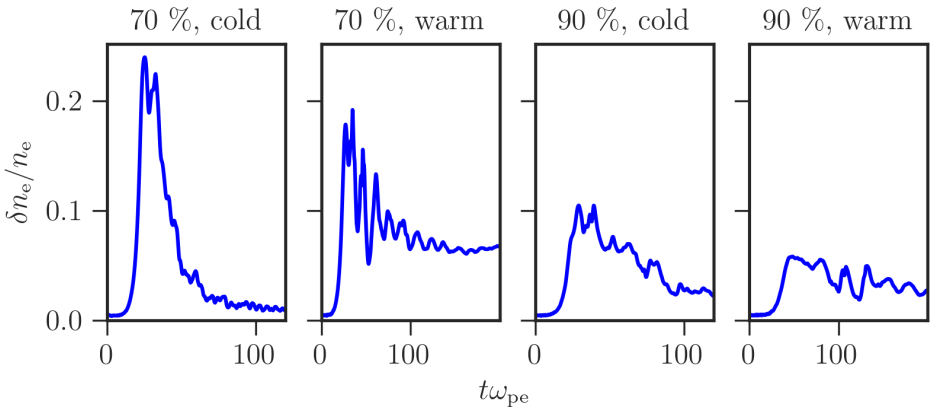

Figure 3.8: Root mean square density fluctuations relative to the average density for the four different cases. As the ring becomes more and more closed, the perturbations become smaller and smaller. Note that the range on the time axis differs between the panels.

and $x_{max} \approx 1c\omega_{pe}^{-1}$, returns to its original x position after a time of $t \approx 20\omega_{pe}^{-1}$, due to the periodicity of the simulation domain. To make sure this does not impact the qualitative result, we simulated the cold 70 % case and 90 % case with doubled box size and doubled number of cells in each direction, keeping the same number of particles per cell (not shown in separate figures). Then, consistently with previous results (Ghizzo *et al.*, 1988), the number of holes doubled. For the 70 % case it also becomes clearer that it does not evolve into a ring. However, the 90 % case still evolves into a ring.

Using a different boundary condition could affect the result. For example, Zhang *et al.* (2019, S1) finds that for a Maxwellian distribution (linearly polarized laser), streaming instabilities can be driven by streams formed by the reflections from the sheath. This should also be the case for the ring distribution, but is outside the scope of this thesis.

Chapter 4

Effects of Collisions on the Weibel Instability

In this chapter, we will consider the effects of collisions on the Weibel instability. We will examine the case when the electron distribution function is a bi-Maxwellian, and the anisotropy is of order unity. We start by describing the simulation setup, and the methods used to calculate growth rates numerically and semi-analytically. Finally, we investigate the effect of collisions on otherwise the same setup. We compare results with previously known analytical results, and find good agreement. Using the previous analytical model combined with our calculation of the growth rate, we give a brief outlook on collisional effects on the Weibel instability in laboratory plasmas.

4.1 Simulation Setup

We use Smilei (Derouillat *et al.*, 2018) for the PIC simulations of the bi-Maxwellian distributions. The simulations are performed in 2D3P. The bi-Maxwellian is initialized with

$$T_\parallel \equiv m_e \left\langle v_z^2 \right\rangle_{\mathrm{e}}^{\mathrm{part}} = 1.5\,\mathrm{keV}, \tag{4.1}$$

and

$$T_\perp \equiv m_e \left\langle v_x^2 \right\rangle_{\mathrm{e}}^{\mathrm{part}} = m_e \left\langle v_y^2 \right\rangle_{\mathrm{e}}^{\mathrm{part}} = 5\,\mathrm{keV}. \tag{4.2}$$

Thus, the distribution function in velocity space is given by

$$f(v_x, v_y, v_z) = n_{\mathrm{e}} \frac{m_e^{3/2}}{2\pi T_\perp \sqrt{2\pi T_\parallel}} \exp\left(-m_e \frac{v_x^2 + v_y^2}{2T_\perp}\right) \exp\left(-m_e \frac{v_z^2}{2T_\parallel}\right), \tag{4.3}$$

where m_e is the electron mass and n_e is the electron density[1]. The distribution has no imposed spatial dependence at the initialization, although the randomness of the macro-particle locations are sufficient as seed fluctuations. When we use collisions in our simulations, we scan the density to explore the impact of collisions. Without collisions, we can normalize the time coordinate to ω_{pe} and then the density does not appear explicitly.

The simulation box is taken to be $1000\lambda_{D\parallel} \times 50\lambda_{D\perp}$ where $\lambda_{D\parallel}$ is defined from $T_\parallel$ and $\lambda_{D\perp}$ is defined from $T_\perp$. We divide the box into 8192×512 cells, and initialize with 50 macro particles per cell and species. In order to reduce storage requirements, we only output field data from every 128^{th} point and 16^{th} point in the parallel and transverse directions, respectively, yielding a 64×32 output grid.

Both electrons and ions are given random initial positions and velocities. The ions are either He^+ or He^{2+} with an isotropic temperature of 1.5 keV. In reality, helium would be fully ionized at temperatures in the keV range. However, by varying the charge, we obtain another way to vary the collision frequency.

For each setup, a total of three simulations are performed. These are done to reduce the impact of the specific form of the initial seed, as we have placed the particles with random initial positions and velocities. A random placement corresponds to that the number of particles in a given volume follow the binomial distribution. For large number of particles in the volume, this is very close to a normal distribution, meaning we seed with almost white noise.

Simulations last for at least $300\omega_{pe}^{-1}$, and the time step is approximately 58 % of the CFL time. How long each of the simulations lasts is given in table 4.1. Note that the growth rates are very small compared to the plasma frequency, forcing the long simulation times. Since the Weibel growth rate is lower (relative to ω_{pe}) for higher densities (higher collision frequency), the simulations are run longer at higher densities.

4.2 Analysis of Growth Rates

In this section, we will go through how we calculate the different growth rates. We will start by explaining how the growth rates are calculated from the simulations, and then cover how we compute the semi-analytical solutions. Finally, we compare the semi-analytical growth rates with the growth rates from the collisionless simulations.

[1]We simulate in two spatial dimensions, so the density in the simulations is a surface density. To achieve the 3D density, the macro-particles are weighted to represent a line density instead of a number of particles.

Table 4.1: Simulation parameters used for each value of the density n_e. The first column shows the density, the second column the ion charge, and the last column the simulation times.

n_e (cm^{-3})	Z	Simulation Time (ω_{pe}^{-1})
–	–	300
1×10^{18}	1	300
1×10^{20}	1	300
1×10^{22}	1	300
1×10^{22}	2	400
1×10^{23}	1	400
1×10^{23}	2	400
1×10^{24}	1	400
1×10^{26}	1	500

4.2.1 Numerical Computation of Growth Rates

To find the growth rates numerically, we fit an exponential to the spectral representation of the observed magnetic field. We have chosen the simulation box to be in the xz-plane, where the z-direction corresponds to the direction with the lowest temperature.

First we need the wave vector spectral representation of the magnetic field. To obtain the magnetic field fluctuation amplitude as a function of k_z, we first average the magnetic field over x. Then we use SciPy's FFT routine (Virtanen *et al.*, 2020) to obtain the spectral representation of the y component of the magnetic field. Growth rates are obtained by minimizing the L^2 norm between the spectral representation and an unknown exponential function. Minimization is done with SciPy's `minimize` function, where the constant pre-factor as well as the exponential growth rate are free parameters.

We notice that the magnetic field has modes oscillating in time, in addition to a growing mode, as seen in fig. 4.1a. The oscillation frequency is much larger than the growth rate. If an oscillating mode has an amplitude comparable or large compared to the initial growing mode, there will be a large error in the computed growth rate. To reduce the effect of the oscillations, we time-average the spectral representations over $2\omega_{pe}^{-1}$. Moreover, we find that the change in the instantaneous temperature anisotropy caused by the instability lowers the growth rate. Due to these two factors, the time interval in which we minimize the L^2 norm has to be chosen carefully. Therefore, the growth rates are calculated in the beginning of the increase in electromagnetic energy, to find a compromise between the need for large amplitude in the growing mode and having a sufficiently constant instantaneous temperature.

To show these two competing factors, we plot the electromagnetic energy evolution in fig. 4.1a as well as the inverse anisotropy in fig. 4.1b, for the three collisionless simulations. The inverse anisotropy is given by

$$A^{-1} \equiv \frac{T_{\parallel}}{T_{\perp}}, \tag{4.4}$$

and is thus a measure on the change in instantaneous temperature. In these simulations, the energy starts rising at the time $t\omega_{\mathrm{pe}} \approx 150$. Already at $t\omega_{\mathrm{pe}} = 250$, the anisotropy has changed visibly, and at $t\omega_{\mathrm{pe}} \approx 300$ the change is substantial. At $t \approx 200\omega_{\mathrm{pe}}$, we find a good compromise between constant anisotropy, and sufficiently large growing-mode amplitude.

We noticed that the growing modes seed fluctuation level is different in different simulations, due to the random placement of particles. Therefore, a time shift is performed to make the electromagnetic energy graphs match. This is done by shifting time such that the energy curves overlap at the end of the simulations, when the impact of the oscillations is the smallest. With this time shift, the energy curve in the different simulations follow each other, apart from the early, oscillation domination, parts of the simulations. Note that more (macro-)particles reduces the initial seed fluctuations.

For each simulation setup, we have done three simulations. The only difference between these simulations is the initial positions and initial velocities of the macroparticles, due to their random initialization. We estimated the error with the standard deviation, given by

$$\sigma^2 = \frac{1}{2}\sum_{i=1}^{3}(\gamma_i(k) - \bar{\gamma}(k))^2, \tag{4.5}$$

where

$$\bar{\gamma}(k) = \frac{1}{3}\sum_{i=1}^{3}\gamma_i(k), \tag{4.6}$$

and $\gamma_i(k)$ is the calculated growth rate for simulation i, as a function of wave vector. The error bars plotted in the graphs throughout this chapter represents this standard deviation. This estimate might, however, not be very accurate, given the small sample size.

4.2.2 Semi-Analytical Solutions to the Plasma Dispersion

To find the roots of the plasma dispersion relation given by eq. (2.48), we implemented a Newton solver[2] in the programming language C. The solver uses the

[2]The solver is available from `https://github.com/albjohan/NSWeibel2Diso`.

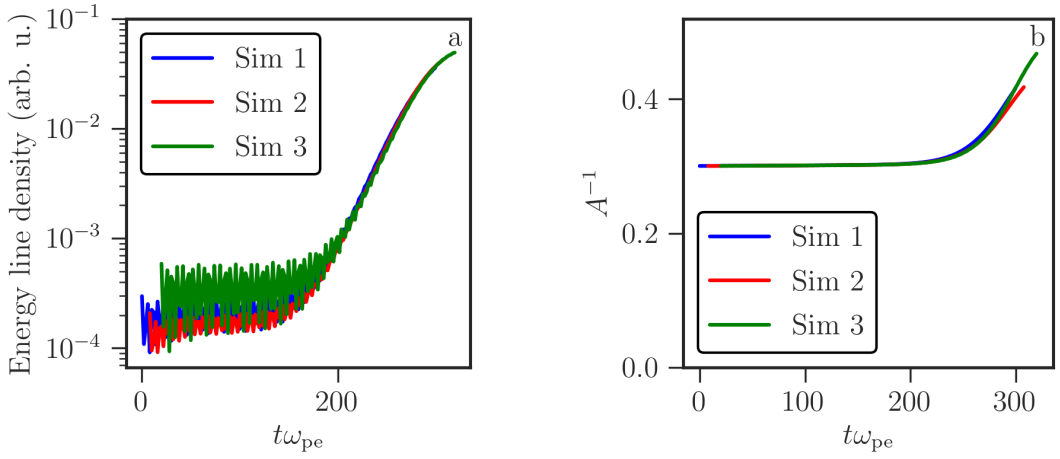

Figure 4.1: In panel (a), we show the total electromagnetic energy for the collisionless simulations. We have shifted the time such that the energy graphs match that of the final time step of the simulation reaching the lowest electromagnetic energy. This is done since the initial positions are random, and thus the time at which the simulation reaches the end of linear phase is also random. With this in mind, we see that the growth of electromagnetic energy is very similar in the three cases. In panel (b), we show the inverse anisotropy versus the shifted time. The inverse anisotropy is given by $A^{-1} = T_{\parallel}/T_{\perp}$, and it changes significantly before the growth in electromagnetic energy has ended (which is after the simulation ends).

normalization given by $c = 1$ and $\omega_{\mathrm{pe}} = 1$. We solve $\epsilon_{xx} = 0$ from eq. (2.48), in the limit where the ion dynamics is negligible, in other words, the sums only include the electron species. The general concept of a Newton solver is to iterate with

$$x_{n+1} = x_n - \frac{f(x_n)}{f'(x_n)}, \tag{4.7}$$

where f is the function whose zeros we want to find. The solver uses the variable $\omega = ip$. The derivative of ϵ_{xx} w.r.t. ω is

$$\epsilon'_{xx}(\omega) = 2\omega - \frac{A}{kv_{\mathrm{th}z}}(2\zeta + (2\zeta^2 - 1)Z(\zeta)), \tag{4.8}$$

where $A = T_\perp/T_\parallel$ is a measure of the anisotropy, $\zeta = \omega/(k\sqrt{2\left\langle v_z^2\right\rangle_{\mathrm{e}}^{\mathrm{part}}})$, and Z is the plasma dispersion function. Equation (2.48) is valid for a Maxwellian distribution in v_z and we thus have that $v_{\mathrm{th}z} \equiv \sqrt{2T_\parallel/m_{\mathrm{e}}}$. It is valid for any distribution in v_x, as long as v_x and v_z are independent. At each step, the new value is given by

$$\omega_{n+1} = \omega_n - \frac{\omega_n^2 - k^2 - 1 + A(1 + \zeta_n Z(\zeta_n))}{2\omega_n - \frac{A}{kv_{\mathrm{th}z}}(2\zeta_n + (2\zeta_n^2 - 1)Z(\zeta_n))}. \tag{4.9}$$

To calculate $Z(\zeta)$, we use the identity

$$Z(\zeta) = i\sqrt{\pi}\exp\left(-\zeta^2\right)[1 + i\,\mathrm{erfi}(\zeta)], \tag{4.10}$$

where $\mathrm{erfi}(\zeta)$ is the imaginary error function. The standard math library is used to calculate $\exp(-\zeta^2)$ for complex numbers, and `libcerf` (Johnson & Wuttke) is used to calculate $\mathrm{erfi}(\zeta)$. Starting points for the iteration are chosen on a uniform 3D grid in (ω, γ, k) space. The user determines which ranges are covered, and how dense the grid is. We have scanned in ranges of $0 < \omega < 2$, $0 < \gamma < 2$ and $0 < k < 200$, with various density. Typically, we have used 100 points in each direction and reduced the maximum values scanned successively.

4.2.3 Comparison Between Numerical and Analytical Results

The comparison of numerical and analytical growth rates as a function of k is shown in fig. 4.2. Semi-analytical solutions for $T_\parallel = 1.5\,\mathrm{keV}$ and $T_\perp = 5\,\mathrm{keV}$ are shown with the red solid line. Growth rates from the simulations are calculated in the interval $t\omega_{\mathrm{pe}} \in [190, 210]$ (blue circles) as well as $t\omega_{\mathrm{pe}} \in [210, 230]$ (green diamonds), where t is the shifted time. There is a slight shift towards lower growth rates at the later time interval, which can be explained by the small reduction in

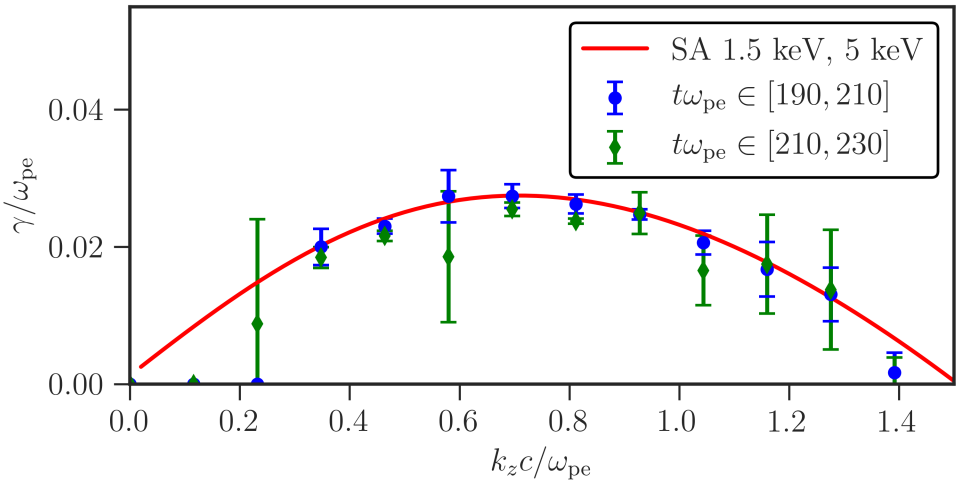

Figure 4.2: Growth rate from simulations in blue circles and green diamonds, calculated as described in section 4.2.1 in different time intervals, and semi-analytical growth rate in the linear limit in red line, calculated as described in section 4.2.2. Difference between the growth rates calculated for $t\omega_{\rm pe} \in [190, 210]$ (blue circles) and $t\omega_{\rm pe} \in [210, 230]$ (green diamonds) could possibly be due to the change in anisotropy.

anisotropy. Linear theory and simulations are found to agree well, within the accuracy of the PIC simulations.

Note that the growth rates from the simulations at the smallest non-zero wave numbers are significantly smaller than the analytical prediction (red curve). That the numerical estimate for γ at $kc/\omega_{pe} \approx 0.25$ is essentially zero in the first time interval (blue circle), and it is comparable to (but still smaller than) the theoretical value in the second time interval (green diamond), indicates that it took a longer time for this mode to grow to significant amplitudes to be suitable for a growth rate estimate. In the simulations performed, we observe a trend that the initial magnetic field energy seed increases with increasing k. The late growth of the modes caused by the weak seeding at low k is causing the apparent discrepancy between the simulated and analytical growth rates.

4.3 Collisional Effects on the Weibel Instability Growth

In this section, we examine numerically the effect of collisions on the Weibel instability, in the presence of anisotropic electron distributions. The collision model used is the one implemented in Smilei (Derouillat *et al.*, 2018), developed by Nanbu (1997) and Nanbu & Yonemura (1998). It is further improved by Perez *et al.* (2012). We include both electron–ion, as well as electron–electron collisions. The density and ion charge are varied between the simulations, yielding different collision frequencies. As collisions depend differently on the density compared to the collisionless Weibel growth rate, it is no longer possible to remove the explicit density dependence by normalizing to the plasma frequency.

4.3.1 Collisional stabilization of the Weibel Instability

We vary the electron density and ion charge to find when collisions dominate the Weibel instability completely. The maximum growth rate versus the collision frequency, ν (eq. (2.60)), is shown in fig. 4.3. Numerical growth rates are shown by the blue diamonds. The maximum growth rate from the semi-analytical solution is shown with the red line. We show the correction derived in Wallace *et al.* (1987), eq. (2.59), with a dashed green line. Note that we do not use their collisionless analytical solution of the growth rate, but rather the solution from our semi-analytical solver. The collisionless growth rate they give has a small discrepancy compared to our semi-analytical solution. Our simulations confirm their theoretical estimate of the collisional effect on the Weibel instability. Using $Z = 2$, we find that in this setting, the Weibel instability is stabilized at $n_e \approx 2 \times 10^{24}\,\mathrm{cm}^{-3}$, corresponding to $\nu/\omega_{\mathrm{pe}} \approx 0.039$.

When the growth rate was derived analytically, the initial value problem was considered. What we choose as our initial time in the analytical calculation is arbitrary, as long as the perturbations are small at that time. The collisions have reduced the anisotropy at the time for which we calculate the growth rate numerically, in addition to directly lowering the growth rate. Therefore, the initial seed in our simulations is of higher importance for higher collision frequencies, which could be the cause for the large error at the second highest collision frequency. However, for the highest collision frequency considered, collisions reduce the growth rate so much that the growing mode never becomes visible. In this case, collisions have almost completely isotropized the distribution function at the final time step.

The Krook model is a simple collision model, and differs from the detailed model implemented in Smilei. This could be a possible cause to the difference observed in our numerical simulations to the analytical model. Surprisingly, the

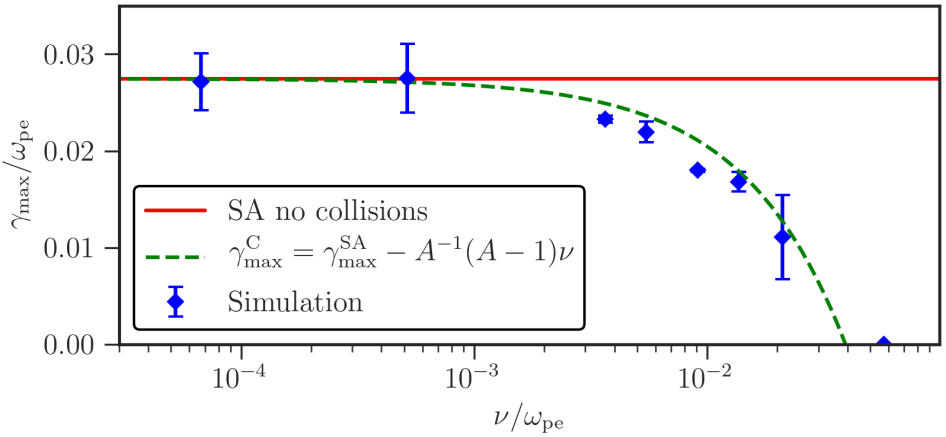

Figure 4.3: Maximum numerical growth rate versus collision frequency. In blue diamonds, the result from the simulations are shown. Semi-analytical solution without collisions is shown with the solid red line, and corrections to it from eq. (2.59) is shown with the dashed green line.

models agree very well. This level of agreement might not be reached with other distribution functions, as the Krook model deforms the distribution function to a Maxwellian distribution exponentially. As we use a bi-Maxwellian distribution, the marginal distribution is Maxwellian for any of the parallel/orthogonal axes (but with a different width).

4.3.2 Outlook on Experiments

Although the parameters in the simulations are experimentally unfeasible (high temperature/density, some cases with unphysical charge), it should be possible to scale the parameters to more experimentally suitable values. As the simulations agree well with the Krook model's prediction, we can expect that the Krook model can give a guideline as to at which collision frequencies we can expect a significant effect on the Weibel growth rate. Note that the simulation parameters were chosen such that they satisfy the CFL criteria, simulate over a time such that $t_{\max}\gamma \gg 1$, and resolve λ_{D}, within the computational cost. If λ_{D} is to be resolved in the PIC simulation, experimentally accessible parameters may not be feasible to simulate using the PIC approach, due to the increasing requirements on the spatial resolution at lower temperatures.

If we scale to an electron density of $5 \times 10^{18}\,\mathrm{cm}^{-3}$, and consider a bi-Maxwellian electron distribution with $T_{\parallel} = 60\,\mathrm{eV}$ and $T_{\perp} = 214\,\mathrm{eV}$, we obtain semi-analytically a collisionless maximum growth rate of $\gamma_{\max} \approx 0.0059\omega_{\mathrm{pe}}$. Using eq. (2.59) with

He^{2+} ions, we find that the corrected maximum growth rate is $\gamma^{\rm C}_{\rm max} \approx -0.0063\omega_{\rm pe}$. In this setting, according to the model, collisions would suppress the Weibel instability. Lowering the density to $10^{17}\,{\rm cm}^{-3}$ instead yields a corrected growth rate of $\gamma^{\rm C}_{\rm max} \approx 0.0036\omega_{\rm pe}$. That is, the Weibel instability is not suppressed completely. It would be interesting if experiments could be carried out, testing the validity of both our simulations and the analytical derivation by Wallace *et al.* (1987).

Chapter 5

Conclusions

In this thesis, we have studied instabilities in plasmas, where the electron distribution is bi-Maxwellian or ring shaped. It is known that a bi-Maxwellian is electrostatically stable, because it decreases monotonically with energy in all directions. In this thesis, we have used linear stability theory to show analytically that 2D ring distributions are stable against electrostatic instabilities. Furthermore, we have also shown that the ring distribution with a small thermal width is also electrostatically stable. The stability of the ring-like distributions is remarkable because of its non-monotonicity (even that of its marginal distributions, unlike for 3D-isotropic distributions) and sharp features in velocity space.

We further find, by employing PIC simulations, that incomplete (anisotropic) rings can collapse to a ring distribution (isotropic) through an electrostatic instability. This electrostatic instability resembles the two-stream instability in phase space, and it is capable of creating BGK modes (Bernstein, Greene & Kruskal, 1957). The resulting non-linear modes have a hole-like structure and they tend to merge until a single phase-space hole is left, consistent with previous results concerning similar structures (Ghizzo *et al.*, 1988; Siminos, Bénisti & Gremillet, 2011). Depending on the gap size in the incomplete rings, we find that they either collapse to closed ring-like distributions, or to a more simple Maxwell-like distribution. Supporting our analytical results, simulations with a complete (isotropic) ring distribution do not generate an instability.

Although the ring-shaped distribution is found to be analytically stable, this thesis studies such distribution functions with periodic boundary conditions, and does not take boundary effects into account. It would therefore be interesting to study these boundary effects theoretically. For example, for a Maxwellian distribution, reflective boundary conditions create streams which drive streaming instabilities (Zhang *et al.*, 2019). This break in isotropy at the boundary should also create streams in the case of a ring distribution.

We also investigate the effects of collisions on the Weibel instability of a bi-

Maxwellian electron distribution, through PIC simulations. Collisions and the Weibel instability compete to isotropize the distribution function. It is found that the direct effect of collisions on the Weibel growth rate agrees well with analytical results using the Krook model (Wallace *et al.*, 1987). For order unity anisotropies, their analytical work predicts that collision frequencies must be comparable to the largest Weibel growth rate in order to suppresses the Weibel instability completely. We have also found that the evolution of the non-fluctuating part of the distribution function is important during the time the instability grows to significant values. Therefore, the initial strength of the seed fluctuations in the beginning of the simulation or experiment can impact the observed growth.

Our results indicate that collisions could play a major role in the Weibel instability in a laboratory setting. It would be very interesting if experiments producing similar anisotropy, e.g. employing the field-ionization method employed by Zhang *et al.* (2019), could test theoretical predictions regarding the suppression of the Weibel instability.

Bibliography

Bernstein, I. B., Greene, J. M. & Kruskal, M. D. 1957 "Exact nonlinear plasma oscillations". *Phys. Rev.* **108**, 546–550, DOI: 10.1103/PhysRev.108.546

Bhatnagar, P. L., Gross, E. P. & Krook, M. 1954 "A model for collision processes in gases. I. Small amplitude processes in charged and neutral one-component systems". *Phys. Rev.* **94**, 511–525, DOI: 10.1103/PhysRev.94.511

Boris, J. P. 1970 "Relativistic plasma simulation-optimization of a hybrid code". In "Proc. Fourth Conf. Num. Sim. Plasmas", (3–67)

Chen, F. 1984 Introduction to plasma physics and controlled fusion. Volume 1: Plasma physics. Plenum Press, New York, NY (United States)

Davidson, R. C. 1983 "Kinetic waves and instabilities in a uniform plasma". In "Basic Plasma Physics: Selected Chapters, Handbook of Plasma Physics, Volume 1", (229)

Derouillat, J., Beck, A., Pérez, F., Vinci, T., Chiaramello, M., Grassi, A., Flé, M., Bouchard, G., Plotnikov, I., Aunai, N., Riconda, C. & Grech, M. 2018 "Smilei: A collaborative, open-source, multi-purpose particle-in-cell code for plasma simulation". *Computer Physics Communications* **222**, 351–373

Ghizzo, A., Izrar, B., Bertrand, P., Fijalkow, E., Feix, M. R. & Shoucri, M. 1988 "Stability of Bernstein–Greene–Kruskal plasma equilibria. Numerical experiments over a long time". *The Physics of Fluids* **31** (1), 72–82, DOI: 10.1063/1.866579

Gradshteyn, I. S. & Ryzhik, I. M. 2007 Table of integrals, series, and products. Elsevier

Horne, R. B., Thorne, R. M., Glauert, S. A., Meredith, N. P., Pokhotelov, D. & Santolík, O. 2007 "Electron acceleration in the Van Allen radiation belts by fast magnetosonic waves". *Geophysical research letters* **34** (17), DOI: 10.1029/2007GL030267

Johnson, S. G. & Wuttke, J. "libcerf, numeric library for complex error functions". https://jugit.fz-juelich.de/mlz/libcerf/. Version [v1.14]

Landau, L. D. 1946 "On the vibrations of the electronic plasma". *Zh. Eksp. Teor. Fiz.* **10**, 25

Lazar, M., Schlickeiser, R., Wielebinski, R. & Poedts, S. 2009 "Cosmological effects of Weibel-type instabilities". *The Astrophysical Journal* **693** (2), 1133–1141, doi: 10.1088/0004-637x/693/2/1133

Marsch, E. 2006 "Kinetic physics of the solar corona and solar wind". *Living Reviews in Solar Physics* **3** (1), 1, doi: 10.12942/lrsp-2006-1

Nanbu, K. 1997 "Theory of cumulative small-angle collisions in plasmas". *Phys. Rev. E* **55**, 4642–4652, doi: 10.1103/PhysRevE.55.4642

Nanbu, K. & Yonemura, S. 1998 "Weighted particles in Coulomb collision simulations based on the theory of a cumulative scattering angle". *Journal of Computational Physics* **145** (2), 639–654, ISSN 0021-9991, doi: https://doi.org/10.1006/jcph.1998.6049

Perez, F., Gremillet, L., Decoster, A., Drouin, M. & Lefebvre, E. 2012 "Improved modeling of relativistic collisions and collisional ionization in particle-in-cell codes". *Physics of Plasmas* **19**, 083 104, doi: 10.1063/1.4742167

Roberg-Clark, G. T., Drake, J. F., Reynolds, C. S. & Swisdak, M. 2016 "Suppression of electron thermal conduction in the high β intracluster medium of galaxy clusters". *The Astrophysical Journal* **830** (1), L9, doi: 10.3847/2041-8205/830/1/l9

Schekochihin, A. A. 2021 Lectures on Kinetic Theory and Magnetohydrodynamics of Plasmas. Oxford University

Siminos, E., Bénisti, D. & Gremillet, L. 2011 "Stability of nonlinear Vlasov-Poisson equilibria through spectral deformation and Fourier-Hermite expansion". *Physical review. E, Statistical, nonlinear, and soft matter physics* **83**, 056 402, doi: 10.1103/PhysRevE.83.056402

Sundström, A., Juno, J., TenBarge, J. M. & Pusztai, I. 2019 "Effect of a weak ion collisionality on the dynamics of kinetic electrostatic shocks". *Journal of Plasma Physics* **85** (1), 905850 108, doi: 10.1017/S0022377819000023

Sundström, A., Gremillet, L., Siminos, E. & Pusztai, I. 2020 "Collisional effects on the electrostatic shock dynamics in thin-foil targets driven by an ultraintense short pulse laser". *Plasma Physics and Controlled Fusion* **62** (8), 085 015, doi: 10.1088/1361-6587/ab9a62

Virtanen, P., Gommers, R., Oliphant, T. E., Haberland, M., Reddy, T., Cournapeau, D., Burovski, E., Peterson, P., Weckesser, W., Bright, J., van der Walt, S. J., Brett, M., Wilson, J., Millman, K. J., Mayorov, N., Nelson, A. R. J., Jones, E., Kern, R., Larson, E., Carey, C. J., Polat, İ., Feng, Y., Moore, E. W., Van-

derPlas, J., Laxalde, D., Perktold, J., Cimrman, R., Henriksen, I., Quintero, E. A., Harris, C. R., Archibald, A. M., Ribeiro, A. H., Pedregosa, F., van Mulbregt, P. & SciPy 1.0 Contributors 2020 "SciPy 1.0: Fundamental algorithms for scientific computing in python". *Nature Methods* **17**, 261–272, DOI: 10.1038/s41592-019-0686-2

Wallace, J., Brackbill, J., Cranfill, C., Forslund, D. & Mason, R. 1987 "Collisional effects on the Weibel instability". *The Physics of fluids* **30** (4), 1085–1088, DOI: 10.1063/1.866305

Weibel, E. S. 1959 "Spontaneously growing transverse waves in a plasma due to an anisotropic velocity distribution". *Phys. Rev. Lett.* **2**, 83–84, DOI: 10.1103/PhysRevLett.2.83

Yee, K. 1966 "Numerical solution of initial boundary value problems involving Maxwell's equations in isotropic media". *IEEE Transactions on antennas and propagation* **14** (3), 302–307, DOI: 10.1109/TAP.1966.1138693

Zhang, C., Huang, C.-K., Marsh, K. A., Clayton, C. E., Mori, W. B. & Joshi, C. 2019 "Ultrafast optical field–ionized gases—a laboratory platform for studying kinetic plasma instabilities". *Science Advances* **5** (9), DOI: 10.1126/sciadv.aax4545. And its supplementary material

Appendix A

Supplementary Material for the Analytical Proof of Electrostatic stability of Ring Distributions

A.1 Finding the Marginal Distribution of the Cold Ring

The marginal distribution is given by

$$f_x(v_x) = \frac{n_\mathrm{e}}{2\pi v_\mathrm{m}} \int_{-\infty}^{\infty} \delta\Big(\sqrt{v_x^2 + v_y^2} - v_\mathrm{m}\Big) \mathrm{d}v_y. \tag{A.1}$$

For any $|v_x| > v_\mathrm{m}$, we have that $\sqrt{v_x^2 + v_y^2} - v_\mathrm{m} > 0$, so

$$\int_{-\infty}^{\infty} \delta\Big(\sqrt{v_x^2 + v_y^2} - v_\mathrm{m}\Big) \mathrm{d}v_y = 0. \tag{A.2}$$

When $|v_x| < v_\mathrm{m}$, we can use the following

$$\int \delta(b(x)) \mathrm{d}x = \sum_{x_0 \in \{x : b(x) = 0, b'(x) \neq 0\}} \frac{1}{|b'(x_0)|}, \tag{A.3}$$

for delta distributions. We let $g(v_y) = \sqrt{v_x^2 + v_y^2} - v_\mathrm{m}$ be the argument to the delta distribution. The derivative is given by $\frac{\mathrm{d}g}{\mathrm{d}v_y} = \frac{v_y}{\sqrt{v_x^2 + v_y^2}}$, which is 0 when $v_y = 0$. We see that $g = 0$ if and only if $v_y = \pm\sqrt{v_\mathrm{m}^2 - v_x^2}$, which is real when $v_x \leq v_\mathrm{m}$. Then,

for $|v_x| < v_\mathrm{m}$ we arrive to

$$f_x(v_x) = \frac{n_\mathrm{e}}{2\pi v_\mathrm{m}} \int_{-\infty}^{\infty} \delta\Big(\sqrt{v_x^2 + v_y^2} - v_\mathrm{m}\Big) \mathrm{d}v_y \tag{A.4}$$

$$= \frac{n_\mathrm{e}}{2\pi v_\mathrm{m}} \sum_{v_y = \pm\sqrt{v_\mathrm{m}^2 - v_x^2}} \left| \frac{\sqrt{v_x^2 + v_y^2}}{v_y} \right| = \frac{n_\mathrm{e}}{\pi} \frac{1}{\sqrt{v_\mathrm{m}^2 - v_x^2}}. \tag{A.5}$$

A.2 Evaluating the Integral in the Dielectric Function for a Cold Ring

We start with eq. (2.32), and consider the case when $\mathrm{Re}(p) > 0$. This is eq. (2.32a), with limits as plus and minus infinity. Before specifying which distribution function we use, we can integrate by parts

$$\int_{-\infty}^{\infty} \frac{f'_{0\alpha}(v_x)}{v_x - i\frac{p}{k}} \mathrm{d}v_x = \left[\frac{f_{0\alpha}(v_x)}{v_x - i\frac{p}{k}} \right|_{-\infty}^{\infty} + \int_{-\infty}^{\infty} \frac{f_{0\alpha}(v_x)}{(v_x - i\frac{p}{k})^2} \mathrm{d}v_x. \tag{A.6}$$

We do not cross any poles since $\mathrm{Re}(p) > 0$. The boundary term is zero since f goes to zero at $\pm\infty$, as it is a distribution function. Now we can substitute the marginal distribution, eq. (3.2), into the expression

$$\int_{-\infty}^{\infty} \frac{f_{0\alpha}(v_x)}{(v_x - i\frac{p}{k})^2} \mathrm{d}v_x = \int_{-v_\mathrm{m}}^{v_\mathrm{m}} \frac{n_\mathrm{e}}{\pi} \frac{1}{\sqrt{v_\mathrm{m}^2 - v_x^2}} \frac{1}{(v_x - i\frac{p}{k})^2} \mathrm{d}v_x. \tag{A.7}$$

The reason why we first integrate by parts and then substitute the marginal distribution, is to deal with the delta distribution correctly. Changing variables to $u = v_x/v_\mathrm{m}$, the limits change to -1 and 1. We also multiply with the prefactor in front of the integral in eq. (2.31), to find

$$\frac{\omega_\mathrm{pe}^2}{n_\mathrm{e} k^2} \int_{-v_\mathrm{m}}^{v_\mathrm{m}} \frac{n_\mathrm{e}}{\pi} \frac{1}{\sqrt{v_\mathrm{m}^2 - v_x^2}} \frac{1}{(v_x - i\frac{p}{k})^2} \mathrm{d}v_x = \beta^{-2} \frac{1}{\pi} \int_{-1}^{1} \frac{1}{\sqrt{1 - u^2}} \frac{1}{(u - i\alpha)^2} \mathrm{d}u, \tag{A.8}$$

where we introduced $\alpha = p/(v_\mathrm{m} k)$ and $\beta = v_\mathrm{m} k/\omega_\mathrm{pe}$. This result yields eq. (3.3).

Gradshteyn & Ryzhik (2007, sec. 2.252) suggests the substitution $\xi = -i(u - i\alpha)^{-1}$ to transform the form of the integral. The choice of the $-i$ prefactor is made on purpose. We will later want that $\sqrt{\xi^2} = \xi$ for the principal branch of the square root. It is indeed the $-i$ pre factor that achieves this, since

$$\xi = \frac{-i}{u - i\alpha} = \frac{-i}{u + \mathrm{Im}(\alpha) - i\,\mathrm{Re}(\alpha)} = \frac{\mathrm{Re}(\alpha) - i(u + \mathrm{Im}(\alpha))}{\mathrm{Re}(\alpha)^2 + (u + \mathrm{Im}(\alpha))^2}. \tag{A.9}$$

Now recall that $\alpha = p/(v_{\mathrm{m}}k)$ and that we have chosen the case when $\mathrm{Re}(p) > 0$, which translates directly to $\mathrm{Re}(\alpha) > 0$. Using eq. (A.9), we can see that this implies $\mathrm{Re}(\xi) > 0$, which is the requirement for $\sqrt{\xi^2} = \xi$.

Inverting the relation between ξ and u, we find the relation between the differentials

$$\frac{1}{\xi} = iu + \alpha \Rightarrow \frac{i}{\xi^2}\mathrm{d}\xi = \mathrm{d}u \Rightarrow -i\mathrm{d}\xi = \frac{1}{(u - i\alpha)^2}\mathrm{d}u. \tag{A.10}$$

It removes the $(u - i\alpha)^{-2}$ factor in the integrand, which is the point with the substitution. Now we will need to evaluate the square root in the integrand (in r.h.s. of eq. (3.3)). We find that

$$\frac{1}{\xi} - \alpha = iu \Rightarrow \left(\frac{1}{\xi} - \alpha\right)^2 = -u^2, \tag{A.11}$$

so that ξ times the square root can be expressed as

$$\xi\sqrt{1 - u^2} = \sqrt{\xi^2 + (1 - \alpha\xi)^2} = \frac{\sqrt{((1 + \alpha^2)\xi - \alpha)^2 + 1}}{\sqrt{1 + \alpha^2}}, \tag{A.12}$$

where we first used that $\sqrt{\xi^2} = \xi$ to move it into the square root, and then completed the square in ξ. Inverting and moving the ξ factor to the r.h.s. we find

$$\frac{1}{\sqrt{1 - u^2}} = \frac{\sqrt{1 + \alpha^2}\xi}{\sqrt{((1 + \alpha^2)\xi - \alpha)^2 + 1}}. \tag{A.13}$$

We are now ready to substitute eq. (A.10) and eq. (A.13) into the integral, to obtain

$$\beta^{-2}\frac{1}{\pi}\int_{-1}^{1} \frac{1}{\sqrt{1 - u^2}} \frac{1}{(u - i\alpha)^2}\mathrm{d}u = \beta^{-2}\frac{-i}{\pi}\int_{u=-1}^{u=1} \frac{\sqrt{1 + \alpha^2}\xi}{\sqrt{((1 + \alpha^2)\xi - \alpha)^2 + 1}}\mathrm{d}\xi. \tag{A.14}$$

We note that the nominator is almost the inner derivative of the square root factor. By extracting a factor $(1 + \alpha^2)^{-1/2}$ and then adding and subtracting α in the nominator, we obtain

$$\begin{aligned} &\beta^{-2}\frac{-i}{\pi}\int_{u=-1}^{u=1} \frac{\sqrt{1 + \alpha^2}\xi}{\sqrt{((1 + \alpha^2)\xi - \alpha)^2 + 1}}\mathrm{d}\xi \\ &\qquad = \beta^{-2}\frac{-i}{\pi\sqrt{1 + \alpha^2}}\int_{u=-1}^{u=1} \frac{(1 + \alpha^2)\xi - \alpha + \alpha}{\sqrt{((1 + \alpha^2)\xi - \alpha)^2 + 1}}\mathrm{d}\xi, \end{aligned} \tag{A.15}$$

where $(1+\alpha^2)\xi - \alpha$ is half the inner derivative of the square root. We have that

$$\begin{aligned}\beta^{-2}\frac{-i}{\pi\sqrt{1+\alpha^2}}\int_{u=-1}^{u=1}\frac{(1+\alpha^2)\xi-\alpha}{\sqrt{((1+\alpha^2)\xi-\alpha)^2+1}}\mathrm{d}\xi \\ = \beta^{-2}\frac{-i}{\pi\sqrt{1+\alpha^2}}\left[\sqrt{((1+\alpha^2)\xi-\alpha)^2+1}\right|_{u=-1}^{u=1}.\end{aligned} \tag{A.16}$$

We have arrived to the r.h.s. of eq. (A.12), which, by examining the l.h.s of eq. (A.12), shows that the integral is 0. This finally leads to

$$\begin{aligned}\beta^{-2}\frac{-i}{\pi\sqrt{1+\alpha^2}}\int_{u=-1}^{u=1}\frac{(1+\alpha^2)\xi-\alpha+\alpha}{\sqrt{((1+\alpha^2)\xi-\alpha)^2+1}}\mathrm{d}\xi \\ = \beta^{-2}\frac{-i}{\pi\sqrt{1+\alpha^2}}\int_{u=-1}^{u=1}\frac{\alpha}{\sqrt{((1+\alpha^2)\xi-\alpha)^2+1}}\mathrm{d}\xi,\end{aligned} \tag{A.17}$$

which results in the equality in eq. (3.4).

By substituting $\eta = (1+\alpha^2)\xi - \alpha$, we find

$$\begin{aligned}\beta^{-2}\frac{-i}{\pi\sqrt{1+\alpha^2}}\int_{u=-1}^{u=1}\frac{\alpha}{\sqrt{((1+\alpha^2)\xi-\alpha)^2+1}}\mathrm{d}\xi \\ = \beta^{-2}\frac{-i\alpha}{\pi(1+\alpha^2)^{3/2}}\int_{u=-1}^{u=1}\frac{1}{\sqrt{1+\eta^2}}\mathrm{d}\eta,\end{aligned} \tag{A.18}$$

where we now see that the integrand is the derivative of $\sinh^{-1}(\eta)$. To know that $\sinh^{-1}(\eta)$ is analytical on our integration path, we need to analyze the path in the complex plane. Expressing η as a function of u, we find

$$\begin{aligned}\eta &= -i\frac{1+\alpha^2}{u-i\alpha} - \alpha \\ &= -i\frac{1+\operatorname{Re}(\alpha)^2 - \operatorname{Im}(\alpha)^2 + 2i\operatorname{Re}(\alpha)\operatorname{Im}(\alpha)}{u+\operatorname{Im}(\alpha) - i\operatorname{Re}(\alpha)} - \operatorname{Re}(\alpha) - i\operatorname{Im}(\alpha).\end{aligned} \tag{A.19}$$

Algebraic simplification yields

$$\begin{aligned}\eta =& \frac{\operatorname{Re}(\alpha)(1-u^2)}{(u+\operatorname{Im}(\alpha))^2+\operatorname{Re}(\alpha)^2} \\ & - i\frac{(1+u^2)\operatorname{Im}(\alpha) + u(1+\operatorname{Re}(\alpha)^2+\operatorname{Im}(\alpha)^2)}{(u+\operatorname{Im}(\alpha))^2+\operatorname{Re}(\alpha)^2}.\end{aligned} \tag{A.20}$$

We see that $\mathrm{Re}(\eta) > 0$ for u in $(-1, 1)$, if $\mathrm{Re}(\alpha) > 0$. Since $\alpha = p/(v_{\mathrm{m}}k)$ and we have chosen $\mathrm{Re}(p) > 0$, it follows that $\mathrm{Re}(\alpha) > 0$. Thus we do not pass the branch cuts of $\sinh^{-1}$, and we obtain

$$\begin{aligned}\beta^{-2}\frac{-i\alpha}{\pi(1+\alpha^2)^{3/2}}\int_{u=-1}^{u=1}\frac{1}{\sqrt{1+\eta^2}}\mathrm{d}\eta \\ = \beta^{-2}\frac{-i\alpha}{\pi(1+\alpha^2)^{3/2}}\left[\sinh^{-1}(\eta)\right|_{u=-1}^{u=1},\end{aligned} \tag{A.21}$$

which is the equality in eq. (3.5).

We can use eq. (A.20) to analyze the limiting behavior of η at the integration limits. For $u = \pm 1$, $\mathrm{Re}(\eta) = 0$. When $u = 1$, we have that

$$\mathrm{Im}(\eta) = -\frac{2\,\mathrm{Im}(\alpha) + 1 + \mathrm{Re}(\alpha)^2 + \mathrm{Im}(\alpha)^2}{(1+\mathrm{Im}(\alpha))^2 + \mathrm{Re}(\alpha)^2} = -1. \tag{A.22}$$

Instead, when $u = -1$, we find

$$\mathrm{Im}(\eta) = -\frac{2\,\mathrm{Im}(\alpha) - 1 - \mathrm{Re}(\alpha)^2 - \mathrm{Im}(\alpha)^2}{(-1+\mathrm{Im}(\alpha))^2 + \mathrm{Re}(\alpha)^2} = 1. \tag{A.23}$$

In addition, $\sinh^{-1}(\eta) = \log\Big(\eta + \sqrt{\eta - i}\sqrt{\eta + i}\Big)$. When $u = \pm 1$, we find that $\sqrt{\eta - i}\sqrt{\eta + i} = 0$. Thus the lower bound is given by $\log(i) = i\pi/2$, and the upper bound is given by $\log(-i) = -i\pi/2$. Finally, we arrive at

$$\left[\sinh^{-1}(\eta)\right|_{u=-1}^{u=1} = i(-\frac{\pi}{2} - \frac{\pi}{2}) = -i\pi, \tag{A.24}$$

so that

$$\beta^{-2}\frac{-i\alpha}{\pi(1+\alpha^2)^{3/2}}\left[\sinh^{-1}(\eta)\right|_{u=-1}^{u=1} = -\beta^{-2}\frac{\alpha}{(1+\alpha^2)^{3/2}}. \tag{A.25}$$

This can be rewritten as

$$-\beta^{-2}\frac{\alpha}{(1+\alpha^2)^{3/2}} = -\frac{\frac{p}{\omega_{\mathrm{pe}}}}{\left(\frac{v_{\mathrm{m}}^2k^2}{\omega_{\mathrm{pe}}^2} + \frac{p^2}{\omega_{\mathrm{pe}}^2}\right)^{3/2}}, \tag{A.26}$$

and can be directly replaced into the the dielectric function (eq. (2.31)). This results in eq. (3.7).

A.3 Integral in Dielectric Function for General 2D-isotropic Distribution

Consider a general isotropic distribution in 2D momentum space $f(v_x, v_y) = f(v_r)$. As the distribution function is 2D isotropic, we can choose the wave vector arbitrarily without loss of generality, and choose it to be in the x-direction. The integral is given by

$$\begin{aligned}\frac{\omega_{\mathrm{pe}}^2}{k^2}\frac{1}{n_{\mathrm{e}}}\int_{-\infty}^{\infty}\frac{\frac{\mathrm{d}f_x(v_x)}{\mathrm{d}v_x}}{v_x - i\frac{p}{k}}\mathrm{d}v_x &= \frac{\omega_{\mathrm{pe}}^2}{k^2}\int_{-\infty}^{\infty}\frac{f_x(v_x)}{\left(v_x - i\frac{p}{k}\right)^2}\mathrm{d}v_x \\ &= \frac{\omega_{\mathrm{pe}}^2}{k^2}\int_{-\infty}^{\infty}\int_{-\infty}^{\infty}\frac{f(v_r)}{\left(v_x - i\frac{p}{k}\right)^2}\mathrm{d}v_y\mathrm{d}v_x,\end{aligned} \tag{A.27}$$

where we first integrated by parts and then used that the marginal distribution is given by

$$f_x(v_x) = \int_{-\infty}^{\infty} f(v_r)\mathrm{d}v_y, \tag{A.28}$$

where $v_r = \sqrt{v_x^2 + v_y^2}$. The boundary term from partial integration is 0 as f is a distribution function, which means that it, along with its derivatives, tends to 0 at $\pm\infty$. We can express f in terms of a convolution with a delta distribution and itself,

$$f(v_r) = \int_0^{\infty}\delta(v_{\mathrm{m}} - v_r)f(v_{\mathrm{m}})\mathrm{d}v_{\mathrm{m}}. \tag{A.29}$$

Using this trick, the integral becomes

$$\begin{aligned}&\frac{\omega_{\mathrm{pe}}^2}{k^2}\frac{1}{n_{\mathrm{e}}}\int_{-\infty}^{\infty}\int_{-\infty}^{\infty}\frac{f(v_r)}{\left(v_x - i\frac{p}{k}\right)^2}\mathrm{d}v_y\mathrm{d}v_x \\ &\qquad = \frac{\omega_{\mathrm{pe}}^2}{k^2}\frac{1}{n_{\mathrm{e}}}\int_{-\infty}^{\infty}\int_{-\infty}^{\infty}\int_0^{\infty}\frac{f(v_{\mathrm{m}})\delta(v_{\mathrm{m}} - v_r)}{\left(v_x - i\frac{p}{k}\right)^2}\mathrm{d}v_{\mathrm{m}}\mathrm{d}v_y\mathrm{d}v_x.\end{aligned} \tag{A.30}$$

We would now like to interchange integration order so that we can use our cold ring results. To do this, we invoke Fubini's theorem. It holds for $\mathrm{Re}(p) \neq 0$, since then the denominator, $(v_x - ip/k)^2$, is never 0. Then, the absolute value of $1/(v_x - ip/k)^2$ acquires a maximum, and thus the integral must be less than a

constant times the integral over f, which is finite. Thus Fubini's theorem holds, allowing us to interchange the order of the integrals, to obtain

$$\begin{aligned}\frac{\omega_{\mathrm{pe}}^2}{k^2}\frac{1}{n_{\mathrm{e}}}\int_{-\infty}^{\infty}\int_{-\infty}^{\infty}\int_{0}^{\infty}\frac{f(v_{\mathrm{m}})\delta(v_{\mathrm{m}}-v_r)}{\left(v_x-i\frac{p}{k}\right)^2}\mathrm{d}v_{\mathrm{m}}\mathrm{d}v_y\mathrm{d}v_x \\ =\int_0^{\infty}f(v_{\mathrm{m}})\frac{\omega_{\mathrm{pe}}^2}{k^2}\frac{1}{n_{\mathrm{e}}}\int_{-\infty}^{\infty}\int_{-\infty}^{\infty}\frac{\delta(v_{\mathrm{m}}-v_r)}{\left(v_x-i\frac{p}{k}\right)^2}\mathrm{d}v_y\mathrm{d}v_x\mathrm{d}v_{\mathrm{m}}.\end{aligned} \tag{A.31}$$

We can now use what we found from the cold ring to evaluate the $\mathrm{d}v_x\mathrm{d}v_y$ integral to

$$\begin{aligned}\int_0^{\infty}f(v_{\mathrm{m}})\frac{\omega_{\mathrm{pe}}^2}{k^2}\frac{1}{n_{\mathrm{e}}}\int_{-\infty}^{\infty}\int_{-\infty}^{\infty}\frac{\delta(v_{\mathrm{m}}-v_r)}{\left(v_x-i\frac{p}{k}\right)^2}\mathrm{d}v_y\mathrm{d}v_x\mathrm{d}v_{\mathrm{m}} \\ =-\int_0^{\infty}\frac{2\pi v_{\mathrm{m}}}{n_{\mathrm{e}}}f(v_{\mathrm{m}})\frac{\frac{p}{\omega_{\mathrm{pe}}}}{\left(\frac{v_{\mathrm{m}}^2k^2}{\omega_{\mathrm{pe}}^2}+\frac{p^2}{\omega_{\mathrm{pe}}^2}\right)^{3/2}}\mathrm{d}v_{\mathrm{m}}.\end{aligned} \tag{A.32}$$

Finally, by changing notation from v_{m} to v_r in the last integral we obtain that

$$\boxed{\frac{\omega_{\mathrm{pe}}^2}{k^2}\frac{1}{n_{\mathrm{e}}}\int_{-\infty}^{\infty}\frac{\frac{\mathrm{d}f_x}{\mathrm{d}v_x}}{v_x-i\frac{p}{k}}\mathrm{d}v_x=-\frac{2\pi}{n_{\mathrm{e}}}\int_0^{\infty}f(v_r)\frac{\frac{p}{\omega_{\mathrm{pe}}}}{\left(\frac{v_r^2k^2}{\omega_{\mathrm{pe}}^2}+\frac{p^2}{\omega_{\mathrm{pe}}^2}\right)^{3/2}}v_r\mathrm{d}v_r.} \tag{A.33}$$

A.4 Dielectric Function for Warm Ring Distribution

We create the warm ring with a rotated Maxwellian,

$$f(v_x,v_y)=N\exp\left(-\frac{\left(\sqrt{v_x^2+v_y^2}-v_{\mathrm{m}}\right)^2}{v_d^2}\right), \tag{A.34}$$

where N is the normalization constant such that the distribution integrates to n_{e}, v_{m} is the speed at which the distribution function attains its maximum (the mode speed), and v_d corresponds to the thermal width of the distribution around the mode speed. The normalization constant is

$$N=\frac{n_{\mathrm{e}}}{2\pi}\left\{\frac{v_d^2}{2}\exp\left(-\frac{v_{\mathrm{m}}^2}{v_d^2}\right)+\frac{v_{\mathrm{m}}v_d}{2}\sqrt{\pi}\left[1+\mathrm{erf}\left(\frac{v_{\mathrm{m}}}{v_d}\right)\right]\right\}^{-1}. \tag{A.35}$$

By inspecting eq. (3.8), we can note that the factor multiplying f has a primitive function in v_r given by

$$\chi(v_r) = \frac{\frac{p}{\omega_{\mathrm{pe}}}}{\sqrt{\frac{v_r^2 k^2}{\omega_{\mathrm{pe}}^2} + \frac{p^2}{\omega_{\mathrm{pe}}^2}}}, \tag{A.36}$$

up to a constant factor. With χ, we can express v_r as

$$v_r = \frac{p}{k}\sqrt{\frac{1}{\chi^2} - 1}. \tag{A.37}$$

We have that

$$\frac{\mathrm{d}\chi}{\mathrm{d}v_r} = -\frac{k^2}{\omega_{\mathrm{pe}}^2} \frac{\frac{p}{\omega_{\mathrm{pe}}} v_r}{(\frac{v_r^2 k^2}{\omega_{\mathrm{pe}}^2} + \frac{p^2}{\omega_{\mathrm{pe}}^2})^{\frac{3}{2}}}. \tag{A.38}$$

The limits are given by $\chi \to 0$ as $v_r \to \infty$, and $\chi = 1$ for $v_r = 0$. Substituting to χ in the integral in eq. (3.8), we obtain

$$\frac{2\pi}{n_{\mathrm{e}}} \int_0^\infty f(v_r) \frac{\frac{p}{\omega_{\mathrm{pe}}}}{\left(\frac{v_r^2 k^2}{\omega_{\mathrm{pe}}^2} + \frac{p^2}{\omega_{\mathrm{pe}}^2}\right)^{3/2}} v_r \mathrm{d}v_r = \frac{2\pi}{n_{\mathrm{e}}} \frac{\omega_{\mathrm{pe}}^2}{k^2} \int_0^1 f\left(\frac{p}{k}\sqrt{\frac{1}{\chi^2} - 1}\right) \mathrm{d}\chi, \tag{A.39}$$

where we have interchanged order of the limits in exchange for the minus sign in the derivative. Inserting the expression for the rotated Maxwellian (eq. (3.9)) yields

$$\frac{2\pi}{n_{\mathrm{e}}} \frac{\omega_{\mathrm{pe}}^2}{k^2} \int_0^1 f\left(\frac{p}{k}\sqrt{\frac{1}{\chi^2} - 1}\right) \mathrm{d}\chi = \frac{2\pi}{n_{\mathrm{e}}} \frac{\omega_{\mathrm{pe}}^2}{k^2} \int_0^1 N \exp\left(-\frac{\left(\frac{p}{k}\sqrt{\frac{1}{\chi^2} - 1} - v_{\mathrm{m}}\right)^2}{v_d^2}\right) \mathrm{d}\chi. \tag{A.40}$$

We will evaluate the integral by Taylor expanding the exponent to second order at its maximum. As it is analytical in $\mathrm{Re}(p) > 0$, we can evaluate the integral for purely real p and then the result holds for all p with $\mathrm{Re}(p) > 0$. Let

$$g(\chi) = \frac{\left(\frac{p}{k}\sqrt{\frac{1}{\chi^2} - 1} - v_{\mathrm{m}}\right)^2}{v_{\mathrm{d}}^2}, \tag{A.41}$$

be the negative exponent. Then

$$\frac{\mathrm{d}g}{\mathrm{d}\chi} = -\frac{\frac{p}{k}\sqrt{\frac{1}{\chi^2} - 1} - v_{\mathrm{m}}}{v_{\mathrm{d}}^2} \frac{p}{k} \frac{2}{\chi^3 \sqrt{\frac{1}{\chi^2} - 1}}, \tag{A.42}$$

which is zero if and only if

$$\frac{p}{k}\sqrt{\frac{1}{\chi^2}-1}=v_\mathrm{m}. \tag{A.43}$$

The second derivative of g at this point is

$$\begin{aligned}\left.\frac{\mathrm{d}^2 g}{\mathrm{d}\chi^2}\right|_{\frac{p}{k}\sqrt{\frac{1}{\chi^2}-1}=v_\mathrm{m}} &= \frac{2}{v_\mathrm{d}^2}\left.\left(\frac{p}{k}\frac{1}{\chi^3\sqrt{\frac{1}{\chi^2}-1}}\right)^2\right|_{\frac{p}{k}\sqrt{\frac{1}{\chi^2}-1}=v_\mathrm{m}} \\ &= \frac{2}{v_\mathrm{d}^2}\frac{p^4}{v_\mathrm{m}^2 k^4}\left(1+\frac{v_\mathrm{m}^2 k^2}{p^2}\right)^3.\end{aligned} \tag{A.44}$$

Expanding g around its minimum to second order, we find that

$$\begin{aligned}&\frac{2\pi}{n_\mathrm{e}}\frac{\omega_\mathrm{pe}^2}{k^2}\int_0^1 N\exp\left(-\frac{\left(\frac{p}{k}\sqrt{\frac{1}{\chi^2}-1}-v_\mathrm{m}\right)^2}{v_\mathrm{d}^2}\right)\mathrm{d}\chi \\ &\quad\approx \frac{2\pi}{n_\mathrm{e}}\frac{\omega_\mathrm{pe}^2}{k^2}\int_0^1 N\exp\left\{-\frac{1}{v_\mathrm{d}^2}\frac{p^4}{v_\mathrm{m}^2 k^4}\left(1+\frac{v_\mathrm{m}^2 k^2}{p^2}\right)^3\left(\chi-\frac{1}{\sqrt{1+\frac{v_\mathrm{m}^2 k^2}{p^2}}}\right)^2\right\}\mathrm{d}\chi.\end{aligned} \tag{A.45}$$

We now want to extend the integral limits to $\pm\infty$. For this to be accurate, the minimum point should be sufficiently far away from the limits 0 and 1. Sufficiently far away means that $\frac{1}{2}(\chi-\chi_0)^2 g''$ is large. For the lower limit, we have

$$\frac{1}{v_\mathrm{d}^2}\frac{p^4}{v_\mathrm{m}^2 k^4}\left(1+\frac{v_\mathrm{m}^2 k^2}{p^2}\right)^2 = \frac{v_\mathrm{m}^2}{v_\mathrm{d}^2}\left(\frac{p^2}{k^2 v_\mathrm{m}^2}+1\right)^2 \geq \frac{v_\mathrm{m}^2}{v_\mathrm{d}^2}, \tag{A.46}$$

which is always much larger than unity if $v_\mathrm{m}/v_\mathrm{d} \gg 1$. For the upper limit, we instead have

$$\begin{aligned}\frac{1}{v_\mathrm{d}^2}\frac{p^4}{v_\mathrm{m}^2 k^4}\left(1+\frac{v_\mathrm{m}^2 k^2}{p^2}\right)^3\left(1-\frac{1}{\sqrt{1+\frac{v_\mathrm{m}^2 k^2}{p^2}}}\right)^2 &= \frac{v_\mathrm{m}^2}{v_\mathrm{d}^2}\left(\frac{p}{k v_\mathrm{m}}+\frac{v_\mathrm{m} k}{p}\right)^3\left(\sqrt{\frac{p}{v_\mathrm{m} k}}-\frac{\sqrt{\frac{p}{v_\mathrm{m} k}}}{\sqrt{1+\frac{v_\mathrm{m}^2 k^2}{p^2}}}\right)^2 \\ &= \frac{v_\mathrm{m}^2}{v_\mathrm{d}^2}\left(\alpha+\frac{1}{\alpha}\right)^3\left(\sqrt{\alpha}-\frac{\sqrt{\alpha}}{\sqrt{1+\frac{1}{\alpha^2}}}\right)^2,\end{aligned} \tag{A.47}$$

where $\alpha = \frac{p}{v_{\mathrm{m}} k}$. Analyzing the infimum over the set of $\alpha > 0, \quad \alpha \in \mathbb{R}$, we find that

$$\left(\alpha + \frac{1}{\alpha}\right)^3 \left(\sqrt{\alpha} - \frac{\sqrt{\alpha}}{\sqrt{1 + \frac{1}{\alpha^2}}}\right)^2 > 1/4, \tag{A.48}$$

so that for $v_{\mathrm{m}}/v_{\mathrm{d}} \gg 4$ we can safely extend the integral limits, and find

$$\begin{aligned}
&\frac{2\pi}{n_{\mathrm{e}}} \frac{\omega_{\mathrm{pe}}^2}{k^2} \int_0^1 N \exp\left\{ -\frac{1}{v_{\mathrm{d}}^2} \frac{p^4}{v_{\mathrm{m}}^2 k^4} \left(1 + \frac{v_{\mathrm{m}}^2 k^2}{p^2}\right)^3 \left(\chi - \frac{1}{\sqrt{1 + \frac{v_{\mathrm{m}}^2 k^2}{p^2}}}\right)^2 \right\} \mathrm{d}\chi \\
&\quad \approx \frac{2\pi}{n_{\mathrm{e}}} \frac{\omega_{\mathrm{pe}}^2}{k^2} \int_{-\infty}^{\infty} N \exp\left\{ -\frac{1}{v_{\mathrm{d}}^2} \frac{p^4}{v_{\mathrm{m}}^2 k^4} \left(1 + \frac{v_{\mathrm{m}}^2 k^2}{p^2}\right)^3 \chi^2 \right\} \mathrm{d}\chi \\
&\quad = \frac{2\pi^{3/2} N v_d v_{\mathrm{m}}}{n_{\mathrm{e}}} \frac{\omega_{\mathrm{pe}}^2}{k^2} \frac{k^2}{p^2 \left(\frac{1 + v_{\mathrm{m}}^2 k^2}{p^2}\right)^{3/2}} \\
&\quad = \frac{2\pi^{3/2} N v_d v_{\mathrm{m}}}{n_{\mathrm{e}}} \frac{\frac{p}{\omega_{\mathrm{pe}}}}{\left(\frac{v_{\mathrm{m}}^2 k^2}{\omega_{\mathrm{pe}}^2} + \frac{p^2}{\omega_{\mathrm{pe}}^2}\right)^{3/2}},
\end{aligned} \tag{A.49}$$

where we used the known integral of a Gaussian. This results in eq. (3.14). Note that even though we only considered α real, if the expression is analytical in α and holds for real α, it holds for complex values as well. Though, for which complex α the expansion holds requires a more detailed study.

A.5 Taylor expansion in eq. (3.18)

We have that

$$h(G) = (\beta^2 + G^2)\sqrt{\beta^2 + G^2} + SG, \tag{A.50}$$

$G = \varepsilon - ix$ with $x > 0$ and $\varepsilon > 0$. The principal branch of square root for a complex number $z = y - ix$ is given by

$$\sqrt{y - ix} = \sqrt{\frac{\sqrt{x^2 + y^2} + y}{2}} - i\sqrt{\frac{\sqrt{x^2 + y^2} - y}{2}}, \quad x > 0. \tag{A.51}$$

In our case, we have

$$\begin{aligned}\sqrt{\beta^2+(\varepsilon-ix)^2} &= \sqrt{\beta^2+\varepsilon^2-x^2-2ix\varepsilon} \\ &= \sqrt{\frac{\sqrt{(\beta^2+\varepsilon^2-x^2)^2+4\varepsilon^2x^2}+\beta^2+\varepsilon^2-x^2}{2}} \\ &\quad - i\sqrt{\frac{\sqrt{(\beta^2+\varepsilon^2-x^2)^2+4\varepsilon^2x^2}-(\beta^2+\varepsilon^2-x^2)}{2}}.\end{aligned} \tag{A.52}$$

With this, we may write the imaginary part of $h(\varepsilon - ix)$ as

$$\begin{aligned}\mathrm{Im}(h) = (x^2-\beta^2-\varepsilon^2)&\sqrt{\frac{\sqrt{(\beta^2+\varepsilon^2-x^2)^2+4\varepsilon^2x^2}-(\beta^2+\varepsilon^2-x^2)}{2}} \\ -2\varepsilon x&\sqrt{\frac{\sqrt{(\beta^2+\varepsilon^2-x^2)^2+4\varepsilon^2x^2}+\beta^2+\varepsilon^2-x^2}{2}} - Sx.\end{aligned} \tag{A.53}$$

To be able to Taylor expand to find $\mathrm{Im}(h)=0$, we must have that the solution is found in $x > \beta+\kappa$ for some fixed (in ε) $\kappa > 0$, since otherwise $|\beta^2 - x^2|$ can become arbitrarily small compared to ε. When $0 < x < \sqrt{\beta^2+\varepsilon^2}$, all terms are negative, so there exists no solutions. Now we are looking in the case when $x > \sqrt{\beta^2+\varepsilon^2}$. At $x = \sqrt{b^2+\varepsilon^2}$, we find that

$$\mathrm{Im}(h)\Big|_{x=\sqrt{\beta^2+\varepsilon^2}} = -2\varepsilon^{3/2}(\beta^2+\varepsilon^2)^{3/2} - S\sqrt{\beta^2+\varepsilon^2} < -S\beta. \tag{A.54}$$

Thus, due to the continuity of h, there is a finite distance κ independent of ε such that $\mathrm{Im}(h) < 0$ for $\beta < x < \beta+\kappa$. It is then possible to Taylor expand in ε for $x > \beta+\kappa$, such that $x^2-\beta^2$ is guaranteed to be large compared to ε^2 (and thus x is large compared to ε). Note that for these x,

$$\frac{x^2}{x^2-\beta^2} \tag{A.55}$$

acquires a maximum. Finding eq. (3.18) is a matter of applying standard Taylor expansions to eq. (A.52).